Pomegranate: a segmentation and 3D reconstruction pipeline for fission yeast

Erod Keaton Baybay[1,*], Eric Esposito[1], Silke Hauf[1,*]

[1]Department of Biological Sciences and Fralin Life Sciences Institute, Virginia Tech, Blacksburg, Virginia, USA

[*]Corresponding authors

E-mail: erodb@vt.edu (EKB), silke@vt.edu (SH)

Abstract

Three-dimensional (3D) segmentation of cells in microscopy images is crucial to accurately capture signals that extend across optical sections. Using brightfield images for segmentation has the advantage of being minimally phototoxic and leaving all other channels available for signals of interest. However, brightfield images readily only provide two-dimensional (2D) segmentation. In radially symmetric cells, such as fission yeast and many bacteria, the brightfield 2D segmentation can be computationally extruded into the third dimension. However, current methods make simplifying assumptions that introduce error. Here, we report Pomegranate, a pipeline that performs the extrusion using spheres placed along the topological skeletons of the 2D-segmented regions. The diameter of these spheres adapts to the cell diameter at each position. Thus, Pomegranate accurately represents cells in 3D even if cell diameter varies and regardless of whether a cell is straight, bent or curved. We have tested Pomegranate on fission yeast and demonstrate its ability to 3D segment wild-type cells as well as classical size and shape mutants. The pipeline is available as macro for the open-source image analysis software Fiji/ImageJ. 2D segmentations created within or outside Pomegranate can serve as input, thus making this a valuable extension to the image analysis portfolio already available for fission yeast and other rod-shaped cell types.

Introduction

Microscopy is a powerful technique to collect spatial and temporal information on cellular processes. However, collecting quantitative data from microscopy images represents a persistent bottleneck. This task is greatly aided by automated or semi-automated image analysis pipelines[1-3]. Automation minimizes subjectivity in the analysis, saves time, and allows for the quantification of more cells than manual analysis. This increases statistical power and provides fine-grained information on cell-to-cell variability.

Annotation of regions of interest (ROIs) can be performed either in two dimensions (X/Y, 2D) or three dimensions (X/Y/Z, 3D). Analysis in 3D becomes important when objects of interest stretch across more than one optical section. Different strategies have been used for 3D segmentation. A popular approach is the use of a fluorescent marker to segment cells in individual optical sections and then combine these 2D ROIs into 3D ROIs. This strategy has multiple drawbacks: using a fluorescent marker for live-cell segmentation (i) increases phototoxicity, (ii) limits the number of fluorescent channels available for proteins or structures of interest, and (iii) can cause variability in segmentation when the intensity of the marker fluctuates.

Using brightfield images for segmentation eliminates these problems but comes with another drawback. While brightfield microscopy highlights the cell contour which allows 2D segmentation, 3D information on cell shape is not readily available. Hence, additional methods are required to extend a 2D ROI into 3D. When the cells being imaged are radially symmetric (e.g. rod-shaped), this information can be used to infer the shape in 3D from that in 2D. Examples for cells with such shape are many bacteria (e.g. *E. coli* or *B. subtilis*) as well as some fungi (e.g. fission yeast).

Fission yeast *(Schizosaccharomyces pombe*) is a eukaryotic model organism frequently used in single-cell imaging studies to gain an understanding of the cell cycle, cell polarity, cell division, and other intracellular signaling events[4,5]. Features that contribute to fission yeast's popularity include its well-annotated, compact genome[6,7], excellent molecular genetics tools[8], and the presence of many genes and pathways that are shared with animals and plants[9,10]. A number of segmentation pipelines based on

46 brightfield imaging have been developed specifically for fission yeast or other rod-shaped
47 cells[11-16] but none of them provides advanced tools for whole-cell 3D segmentation.

48 Here, we present Pomegranate, a pipeline for the 3D segmentation of radially
49 symmetric cells which combines 2D brightfield segmentation with 3D morphological
50 extrapolation. We validate Pomegranate using fission yeast. Unlike previous extra-
51 polation approaches (e.g.[17,18]), Pomegranate does not assume cells to be straight, nor
52 does it assume constant cell width. To create the 3D shape, Pomegranate uses spheres
53 with centers located along the central axis of the cell. The diameter of each sphere is
54 taken from the cell width at this position. Thus, Pomegranate accurately projects the
55 variable cell width of a single cell into 3D and performs equally well on bent, curved and
56 straight cells. Pomegranate is expected to work on all cell types that are radially
57 symmetric along a central axis that is parallel to the imaging plane and provides improved
58 3D segmentation for such cells.

Results

59 **3D reconstruction with Pomegranate**

60 We developed Pomegranate to segment fission yeast or similar rod-shaped cells
61 in 3D. As input, the pipeline takes a Z-stack of brightfield images for segmenting the cell
62 and a Z-stack of fluorescence images for segmenting the cell nucleus and any markers
63 of interest (Fig. 1 and 6). Before being added to the pipeline, the images are background-
64 subtracted, flat-field corrected and corrected for axial chromatic aberration as well as for
65 distortions in axial distance (Fig. S1 and S2).

66 Nuclear segmentation is optional in Pomegranate, and nuclei and cells are initially
67 treated separately and later combined. To define the nucleus, Pomegranate uses
68 traditional adaptive thresholding across all optical sections (Fig. 1A). The ROIs from all
69 optical sections are combined to obtain the 3D representation of the nucleus. We used
70 TetR-tdTomato-NLS as the fluorescent marker, which yields a bright signal in the nucleus
71 and a slightly weaker signal in the nucleolus[19].

72 For whole-cell segmentation, Pomegranate uses brightfield images to define a
73 midplane ROI (Fig. 1B). To obtain the midplane ROI, the characteristic intensity pattern
74 surrounding cells in the brightfield image (Fig. S3) is used to define the edges of the cell
75 (Fig. 1B, see Methods for details)[13,15,20]. As an alternative to this brightfield segmentation,
76 externally prepared midplane ROIs can be used. This allows users to run any pipeline of
77 their choice for 2D cell segmentation (e.g.[11,13,14]) while still profiting from Pomegranate's
78 3D reconstruction.

79 The key feature of Pomegranate is extrusion of the cellular midplane ROI into 3D
80 (Fig. 2). Based on the assumption of radial symmetry, Pomegranate extrudes multiple
81 spheres along the length of the cell, whose diameters correspond to the cell width at this
82 position (Fig. 2A-D). ROIs in the optical sections away from the midplane are defined by
83 this extrusion (Fig. 2B,D). The ROIs from all optical sections are then combined to obtain
84 the 3D representation of the cell (Fig. 2E,F). As path for the spheres, Pomegranate uses
85 the 'topological skeleton' (Fig. 1B, panel 5 and 7; Fig. 2C), a line equidistant to the cell
86 boundaries. Since this line follows cell shape, Pomegranate processes straight, bent or
87 curved cells equally well.

88 Finally, if both cell and nuclear segmentation are available, nuclei are assigned to
89 the cells in which they are located. If the Z positions of the cellular and nuclear midplane
90 differ, users have the option to re-assign cellular midplane ROIs to the optical section of
91 the corresponding nuclear midplane. This may be necessary if cells are not all located in
92 the exact same plane.

93 Overall, the core unique step of Pomegranate is the spherical extrusion to obtain
94 the 3D representation of cells (Fig. 2). Beyond that, the pipeline is adaptable to the
95 specific requirements of each individual user.

96 **Pomegranate accurately isolates regions of interest**

97 To assess the ability of Pomegranate to accurately segment cells, we applied the
98 pipeline to cells expressing the nuclear fluorescent marker TetR-tdTomato-NLS in
99 combination with a cytoplasmic fluorescent marker: Mep33-mCherry for a weaker
100 cytoplasmic signal or Mep33-tdTomato for a brighter cytoplasmic signal (Fig. 3A). We
101 used the weaker cytoplasmic signal when segmenting nuclei and the brighter cytoplasmic

102 signal when testing the ability of the 3D cellular segmentation to capture cytoplasmic
103 signals. After segmentation and 3D reconstruction, we analyzed the intensities of voxels
104 either in the full image, or within the ROIs defining nuclei or cells. Pomegranate
105 successfully isolated the higher intensity signals in nucleus or cells from the background
106 signal (Fig. 3B), indicating that Pomegranate segments accurately in 3D.

107 A frequent workaround to proper 3D segmentation is applying the 2D midplane
108 ROI to all optical sections, which is analogous to analyzing a projection of all optical
109 sections (Fig. S4A). This strategy falsely includes extracellular background. The
110 approach can be slightly improved by only including sections above or below the midplane
111 that are likely to be located within the cell (Fig. S4A). Direct comparison of this approach
112 to Pomegranate finds that Pomegranate identifies a narrower distribution of pixel
113 intensities (Fig. S4B), likely reflecting a more accurate capture of cytoplasmic signals. We
114 conclude that the brightfield-based 3D segmentation of Pomegranate is successful in
115 capturing fluorescent cytoplasmic signals and does so with higher accuracy than
116 projection-based approaches.

117 **Pomegranate refines volume measurement in wild-type cells**

118 Segmenting cells in 3D is useful to measure cytoplasmic signals, but also provides
119 information on cell volume, which is an important parameter in cell growth studies. To
120 estimate cell volume, some prior studies have made the approximation that fission yeast
121 cells are cylinders with hemispherical ends (e.g.[17,18,21,22]). Cell length and width
122 measurements from the midplane ROI are used to calculate the volume of this idealized
123 shape. To compare this method to 3D reconstruction by Pomegranate, we imaged wild-
124 type fission yeast cells and analyzed more than 9,000 cells with two variations of this
125 earlier method in addition to Pomegranate. In the two variations, cell length and width are
126 obtained either from the major and minor axis of an elliptical fit or from the maximum and
127 minimum Feret diameter (also called the caliper diameter) of the midplane ROI (Fig. 4A,
128 see Methods for details). We find that cellular volumes obtained by Pomegranate are
129 around 15% smaller (Fig. 4B). Volumes obtained by Pomegranate are also less variable
130 across the cell population (Fig. 4B). This suggests that the methods assuming a straight
131 rod shape tend to overestimate volume and add technical noise. The overlay of example

132 regions shows that the discrepancies largely result from unequal width along the length
133 of the cells (Fig. 4C). In addition, the requirement of the elliptical fit to maintain the area
134 of the original ROI tends to overestimate cell length. Altogether, this analysis suggests
135 that 3D segmentation by Pomegranate improves volume measurements compared to
136 methods that assume a cylinder with hemispherical ends as cell shape.

137 The volume of the nucleus scales with the volume of the cell[17,23] (Fig. S6). The
138 ratio of nuclear to cell volume (the N/C ratio) has been reported to be 8 % in fission yeast
139 when using idealized geometries for both nucleus and cell[17,22]. Electron microscopy
140 experiments measured 9.4 %[24] and 12 %[25]. Similarly, we find an N/C ratio of 10 % (SD =
141 2.5 %) when using volumes from idealized geometries (Fig. S6B). Measured by
142 Pomegranate 3D reconstruction, the N/C ratio is higher (13 %, SD = 3 %, Fig. S6B), as
143 is expected from the smaller cell volume (Fig. 4B). Interestingly, we also find that the N/C
144 ratio is more variable in smaller compared to larger cells (Fig. S6C). This suggests that
145 cell division introduces variability, which may get corrected as cells grow[22,26].

146 Given the difficulties in measuring volume, cell length has sometimes been used
147 as a simple proxy for cell size (e.g.[27,28]). Correlation analysis in our large dataset (Fig. S7)
148 shows that cell volume indeed correlates well with cell length (Pearson $r = 0.89$, $p < 0.01$).
149 However, cell volume also correlates to a lesser yet significant extent with cell width
150 (Pearson $r = 0.59$, $p < 0.01$). The correlation between cell length and cell width is weaker
151 (Pearson $r = 0.26$, $p < 0.01$). This suggests that cell width, which is often ignored,
152 influences cell volume largely independent of cell length and should be accounted for in
153 order to approximate volume. The analysis above further suggests that Pomegranate's
154 ability to take the variation of cell width within individual cells into account improves cell
155 volume estimates.

156 **Pomegranate reconstructs cell size and shape mutants in 3D**

157 While wild-type fission yeast cells have a relatively uniform shape, mutant cells
158 can drastically deviate from this shape[29]. We therefore tested whether Pomegranate can
159 segment cell size and shape mutants. We used *tea1Δ* for curved cells, *wee1-50* for short
160 cells, and *cdc25-22* for long cells[30-32]. Our whole-cell segmentation successfully captured
161 the shape of these mutants (Fig. 5B). We estimated curvature by assessing solidity of the

162 midplane ROI (Fig. 5A). Solidity is defined as the ROI area divided by smallest convex
163 area that contains the ROI (convex hull). Low solidity indicates a concave shape. Wild
164 type and *tea1Δ* cells exhibited mean solidities of 0.94 and 0.93, respectively. The
165 coefficient of variation for *tea1Δ* (CV = SD/Mean = 3 %) was higher than that of wild type
166 (CV = 2 %), suggesting greater variability in cell curvature[30,33]. The *cdc25-22* cells
167 exhibited the lowest mean solidity of 0.87. Because these cells are overly long, even slight
168 curvature leads to large area differences between convex hull and ROI area. The highest
169 solidity was exhibited by *wee1-50* mutant cells (0.95) as their compact geometry prohibits
170 curvature. Our results are highly similar to those obtained by Liu *et al.* in the testing their
171 morphometry toolbox[14]. This validates our 2D segmentation and demonstrates that
172 Pomegranate successfully segments size and shape mutants.

173 As the curvature analysis indicates, these size and shape mutants are not well
174 approximated by assuming cells to be a cylinder with hemispherical ends (Fig. 4A).
175 Pomegranate therefore provides the necessary functionality to measure volume of these
176 mutants. As expected, cell volumes were smaller than for wild type (Mean = 91 μm^3) in
177 *wee1-50* mutants (Mean = 50 μm^3), larger in *cdc25-22* mutants (Mean = 350 μm^3) and
178 most similar to wild type in *tea1Δ* cells (Mean = 110 μm^3, Fig. 5). Assuming an idealized
179 rod shape yielded volumes that were up to about 75 % larger than those obtained from
180 the Pomegranate analysis (e.g. *cdc25*-22 Mean = 622 μm^3 when assuming rod shape
181 and using Feret diameters, Fig. S8). This suggests that the advantages of using
182 Pomegranate for 3D segmentation and volume estimation are even greater when
183 analyzing size and shape mutants.

184 In summary, we conclude that Pomegranate successfully segments wild-type
185 fission yeast cells as well as size and shape mutants in three dimensions (Fig. 3-5) and
186 allows for accurate estimates of volume (Fig. 4). After correcting for axial chromatic
187 aberration, the ROIs across all optical sections can be used to quantify any signal of
188 interest (Fig. 6).

Discussion

189 **Different approaches to 2D segmentation from brightfield images**

190 Using brightfield images for segmentation is appealing because acquiring these
191 images is minimally phototoxic and all fluorescence channels remain available for
192 proteins of interest. Brightfield microscopy yields a consistent intensity pattern along the
193 cell boundary across optical sections (Fig. S3), which we and others have leveraged to
194 obtain a midplane ROI. For example, PombeX[15] identifies this pattern by k-means
195 clustering. MAARs[13] and the MPCS algorithm[12] use correlation analysis. These methods
196 have been further complemented by machine learning[15,34] or neural networks[16]. Other
197 methods do not use the pattern itself, but use traditional segmentation on brightfield
198 images: either edge detection[35] or adaptive thresholding[14]. Our segmentation relies on
199 projection of the pattern and adaptive thresholding supplemented by watershedding and
200 traditional morphometry tactics, which together have the advantage of simplicity, low
201 computational demand, and no need for training data.

202 **Optional user input to Pomegranate**

203 To accommodate for different imaging conditions, several parameters in the 2D
204 segmentation of Pomegranate (Fig. 1) can be changed by the user as specified in the
205 usage guide. For the settings we used, up to 96 % of cells were accurately detected on
206 images with low cell density. This percentage tended to be lower on high cell density
207 images (between 70 and > 90 %). Adjustable filters exclude most false-positive ROIs
208 (such as those capturing background or debris rather than a cell). Any remaining false-
209 positive ROIs can be manually excluded prior to the 3D reconstruction step.

210 Sensitivity of image recognition algorithms to the imaging conditions is a general
211 problem, and we have therefore constructed Pomegranate to be capable of using ROIs
212 obtained by other segmentation methods as input for 3D reconstruction. These
213 segmentations do not need to be performed on a brightfield image. Hence, 3D
214 reconstructions with Pomegranate can also be performed from phase contrast imaging,
215 differential interference contrast imaging, widefield fluorescence microscopy, or confocal

microscopy, provided a 2D detection and segmentation algorithm produces an accurate 2D cell shape as input.

Advantages of 3D segmentation by Pomegranate

Because segmentation in 3D is not trivial, workarounds have often been used. Prominent workarounds are projections (Fig. S4) or approximations of the rod shape as a cylinder with hemispherical ends (Fig. 4). Both of these approaches require a 2D midplane ROI. Pomegranate uses the same midplane ROI but makes optimal use of the information contained in this ROI for 3D extrusion, thereby achieving a more accurate representation of the cell compared to these approaches.

Our analysis indicated that cell width varies along the length of a cell (Fig. 4) and between cells (Fig. S7) and should not be ignored when calculating volume or representing cells in 3D. For the same reason, recent extrusion approaches to measure cell volume and surface area have already started to use techniques that take variations of cell width along the length of the cell into account[36-38]. Pomegranate differs from these methods in that it uses the topological skeleton rather than a straight central axis for extrusion. Pomegranate therefore more accurately represents bent or curved cells in 3D, and particularly excels on shape mutants (Fig. S8). Pomegranate also provides 3D segmentation within the open-source image analysis software Fiji[3] so that signals of interest in other channels can be quantified.

It should be noted that Pomegranate's approach is not without its own simplifying assumptions. Spherical extrusion assumes that the cells are indeed radially symmetric around the long axis, which may not always be the case. For fission yeast, the general notion is supported both by biophysical considerations[39] and by imaging cells cells along the long axis, where they appear round[40,41]. Furthermore, Pomegranate's approach requires that the long axis of cells is parallel to the XY imaging plane. This will typically be the case when cells are imaged in microfluidics channels, but the requirement may not always be met when cells are fixed on glass slides without any constraint in Z.

Pipeline limitations

Pomegranate is currently only compatible with single timepoint images. Using the pipeline for time series images will require analyzing each timepoint individually. Tracking cell movement and division over time is currently not a feature of the pipeline.

Pomegranate calculates surface areas in addition to volume (Fig. S5). However, these areas are calculated from the voxel surfaces which is an overestimation. More accurate values can be obtained by calculating the theoretical surface area from the extruded spheres, but this mathematical step has not yet been implemented.

Summary

Because Pomegranate can work with both externally and internally generated 2D segmentations, we see it not as an alternative but as a valuable extension to the image analysis portfolio that many groups already use. Pomegranate's 3D reconstruction algorithm improves volume estimates and allows for quantification of cellular signals in 3D (Fig. 6). Since the only assumption for the 3D extrusion is radial symmetry around a long axis, Pomegranate is applicable to all cell types with such shape including many rod-shaped bacteria in addition to fission yeast.

Code availability

The software, usage guide, example images, and additional tools are available at the Pomegranate GitHub repository (https://github.com/erodb/Pomegranate). Installation of Pomegranate is possible through a FIJI/ImageJ update site (https://sites.imagej.net/HaufLab) or through direct download of the macro files from GitHub.

Materials and methods

Fission yeast strains

Strain Name	Mating Type	Genotype	Used in
SW184	*h-*	*leu1 Z<<natR<<Padh31-tetR-Tdtomato*	Fig. 4, 5, S2, S3, S5, S6, S7

SW169	*h+*	*Z<<natR<<Padh31-tetR-tdTomato mep33+-mCherry<<hygR*	Fig. 3, S4
SW191	*h+*	*Z<<natR<<Padh31-tetR-tdTomato mep33+-tdTomato<<kanR*	Fig. 3, S4
SW178	*h+*	*mad1+-ymEGFP Z<<natR<<Padh31-tetR-tdTomato*	Fig. 4, S2, S5, S6, S7
SW179	*h+*	*mad1-codonOpt-ymEGFP Z<<natR<<Padh31-tetR-tdTomato*	Fig. 4, S3, S5, S6, S7
SW180	*h+*	*mad2+-ymEGFP Z<<natR<<Padh31-tetR-tdTomato*	Fig. 4, S5, S6, S7
SW181	*h+*	*mad2-codonOpt-ymEGFP Z<<natR<<Padh31-tetR-tdTomato*	Fig. 4, 5, S2, S5, S6, S7
SW182	*h+*	*mad3+-ymEGFP Z<<natR<<Padh31-tetR-tdTomato*	Fig. 4, S5, S6, S7
SW183	*h+*	*mad3-codonOpt-ymEGFP Z<<natR<<Padh31-tetR-tdTomato*	Fig. 4, S2, S3, S5, S6, S7
JX798	*h-*	*ade6-M210 ura4-D18 tea1Δ::ura4+*	Fig. 5, S8
JY327	*h-*	*wee1-50*	Fig. 5, S8
SW323	*h+*	*cut1+-GFP<<kanR cdc25-22*	Fig. 5, S8

The *tea1Δ::ura4+*[30], *wee1-50*[31], *cdc25-22*[32] and *tetR-tdTomato-NLS*[19] alleles have been described, and strains expressing these were obtained from Y. Watanabe. The GFP-tags present in some strains are not relevant for the purpose of this study. Yeast monomeric enhanced GFP (ymEGFP) tagged alleles of *mad1*, *mad2* and *mad3* will be described elsewhere (Esposito et al., in preparation).

Microscopy

Fission yeast cells were revived from frozen stocks on YEA plates (yeast extract with additional 0.15 g/L adenine)[42]. For imaging, cells were inoculated into 7 mL of EMM2 (Edinburgh Minimal Medium, MP Biomedicals # 4110012)[42] with 0.2 g/L leucine or 0.15 g/L adenine added for auxotrophic strains. Cells were grown to a concentration of around 1 x 10^7 cells/mL. Cells were diluted to a concentration of 3 x 10^6 cells/mL and loaded into the cell input wells of a CellASIC ONIX Y04C microfluidics plate. EMM2, with leucine or adenine if needed, was loaded into the media input wells of the microfluidics plate.

Cells were loaded into the imaging window of the microfluidics plate by multiple 5 second pulses of 8 psi. The six media input wells of the microfluidics plate were run in symmetric pairs (1/6, 2/5, and 3/4) to maintain homogenous flow direction. Medium was run at 6 psi.

284 The microfluidics plate was imaged using an inverted widefield DeltaVision
285 Microscope with pco.edge 4.2 (sCMOS) camera, Olympus 60X/1.42 (UIS2, 1-U2B933)
286 objective, Trulight fluorescent illumination module, and EMBL environmental chamber.
287 Imaging was performed at 30˚C (34˚C for fission yeast *cdc25-22* mutants).

288 Multi-channel Z-stack images were collected with 72 or 100 optical sections, at a
289 section spacing of 0.1 µm. With these parameters, a 0.1071 µm (X axis) x 0.1071 µm
290 (Y axis) x 0.1 µm (Z axis) voxel size is generated. Note that axial distances are
291 recalibrated later (Fig. S1, S2). Images were taken at multiple locations within the
292 microfluidics chamber, sampling across a wide range of cell densities.

293 **Image corrections and calibrations**

294 All raw images were deconvolved with three cycles of conservative deconvolution,
295 without any additional deconvolution corrections or normalizations, using softWoRx
296 (Applied Precision). Deconvolved images were subjected to flat-field correction, axial
297 chromatic aberration correction (Fig. S1A,B), and axial distance correction (Fig. S1C-F).

298 Flat-field correction was applied to correct for non-uniform illumination of the
299 imaging field. Images for flat-fielding were acquired by imaging Alexa Fluor-488 and Alexa
300 Fluor-568 labeled antibodies (Invitrogen/Thermo Fisher) diluted 1:100 in PBS and
301 mounted in an 8-well µ-Slide (Ibidi). Flat-field images from different sample positions were
302 averaged to compensate for stochastic differences. Dark noise images were collected by
303 imaging with a closed shutter. Dark noise was subtracted from all flat-field and raw
304 images. Flat-field images were normalized by dividing all pixel intensities by the mean
305 image intensity. Finally, dark noise-subtracted raw images were divided by dark noise-
306 subtracted, normalized flat-field images.

307 In order to correct for axial chromatic aberration (i.e. light of different wavelengths
308 getting focused onto different optical sections), 0.1 µm TetraSpeck Fluorescent
309 Microspheres (Invitrogen/Thermo Fisher) were imaged (Fig. S1A). The beads were
310 viewed from the XZ orthogonal perspective, and the chromatic aberration along the Z axis
311 was quantified in Fiji by manually measuring the distance in pixels between the centers
312 of the bead image in each fluorescent channel (Fig. S1B). Raw images were corrected

313 by shifting the Z position of the optical sections for each channel relative to the other
314 channels based on the measured axial chromatic aberration.

315 We noted that our images had an axial distortion that made round objects appear
316 elliptic in XZ or YZ projections (Fig. S1C,E), presumably a consequence of using a
317 widefield system. In order to correct for this axial distortion, 4 µm TetraSpeck Fluorescent
318 Microspheres were imaged in the same medium that was used for cells (EMM2). The
319 beads were viewed from the XZ orthogonal perspective, and the geometric elongation
320 was quantified manually in Fiji by measuring the width and height of the bead (Fig. S1D).
321 The ratio of these was used as the correction factor. Raw images were corrected by
322 multiplying the Z distance between planes with the correction factor to undo the apparent
323 stretching in Z. Other imaging systems may not require such a correction. When we used
324 TetraSpeck Fluorescent Microsphere pre-mounted on a slide to measure the correction
325 factor, the value was higher (Fig. S1F) and insufficient to lead to a round appearance of
326 nuclei in XZ or YZ. If such a correction is needed, we therefore recommend imaging beads
327 in the same medium as cells, or empirically determining the factor using the assumption
328 that nuclei have a round shape in orthogonal views.

329 Because the strategies for nuclear and whole-cell 3D segmentation are different,
330 nuclear and whole-cell volumes are differently affected by the correction factor (Fig. S2B).
331 The volume of nuclei measured in voxels stays constant but nuclear volume in μm^3
332 changes. In contrast, because cell volume is constructed by extrusion, the cell volume in
333 μm^3 stays constant, regardless of the correction factor, but the number of voxels in the
334 3D ROI changes.

335 **Downstream processing**

336 Compilation, processing, and data visualization of Pomegranate outputs were
337 performed in R[43], using the tidyverse[44], ggpubr[45], ggcorrplot[46], MASS[47] and gridExtra[48]
338 packages.

339 We excluded cells from the analysis that had two nuclei, and we excluded nuclei
340 that were not matched with a cell segmentation (Fig. S2A). For some analyses (Fig. S6),
341 we applied an additional, optional filter that excludes cells if either the cell or the nucleus
342 have an aspect ratio of lower than 0.8 or higher than 1.2 (Fig. S2A). We define the aspect

343 ratio as extension of the region in Z divided by the largest diameter or cell width in X/Y.
344 Aspect ratios of less than 1 occur when a cell is shifted in Z and the collected optical
345 sections do not fully cover the cell volume. Imperfect nuclear acquisition can result in
346 aspect ratios higher than 1.2 (Fig. S2A). In these cases, the nuclear midplane is often
347 asymmetrically located, which may misplace the whole-cell segmentation with respect to
348 the nucleus.

349 **Pipeline development and testing**

350 Pomegranate was written in the macro language of the ImageJ/Fiji open-source
351 imaging processing software[3]. Development and testing was performed on a 2017 iMac
352 (4.2 GHz Intel Core i7 Processor, 16 GB 2400 MHz DDR4 RAM, Catalina Version
353 10.15.5) and a 2018 Mac mini (3 GHz Intel Core i5, 16 GB 2667 MHz DDR4 RAM, macOS
354 Mojave Version 10.14.6).

355 **Nuclear 2D segmentation**

356 Nuclear segmentation was accomplished by using a fluorescent marker enriched
357 in the nucleus (TetR-tdTomato-NLS[19]). Images were taken at multiple optical sections
358 and segmentation was performed on each section. A Gaussian blur and unsharp mask
359 were used to enhance acutance and edge contrast for the nuclei (Fig. 1A, panel 2). An
360 adaptive threshold (Otsu's method[49]) was used to produce a binary image (Fig. 1A, panel
361 3). A Gaussian blur and remasking was used to smooth the binary image (Fig. 1A, panel
362 4). Fiji's "Analyze Particles" algorithm was used to translate the binary image into nuclear
363 ROIs.

364 To eliminate 2D ROIs that deviate too much from the expected idealized circular
365 shape, we calculated circularity, *C* as

366 $$C = 4\pi \frac{A}{P^2}$$

367 where A is the ROI area, and P is the ROI perimeter. ROIs below a circularity of
368 0.6 were excluded by Fiji's "Analyze Particles" algorithm. ROIs with a low circularity
369 typically occurred when the nucleolar signal was too weak and had not been incorporated
370 into the segmentation, resulting in a crescent-shaped region. We further dilated all nuclear

371 ROIs by 0.1 μm, which was necessary to improve acquisition of target fluorophores at the
372 nuclear periphery. Dilation is optional in the pipeline and the extent of dilation can be
373 defined by the user. Finally, an elliptical fit was performed on all nuclear ROIs, to alleviate
374 the impact of irregular shapes resulting from lower nucleolar signals. Elliptical fits convert
375 the ROI into an ellipse where the area, orientation and centroid of the original ROI are
376 preserved.

377 **Nuclear 3D reconstruction**

378 For nuclear reconstruction, ROIs from the nuclear 2D segmentation were grouped
379 by their centroid coordinates to form nuclei. ROIs in adjacent optical sections were
380 grouped when the XY distance between their centroids did not exceed 2.0 μm. To
381 eliminate nuclei that had moved during acquisition, nuclei were excluded if the XY
382 distance of any single centroid to the mean nuclear centroid exceeded 3.0 μm. These
383 threshold values can be changed by the user. In instances where nuclei had intermittent
384 optical sections without ROI, the largest subset of contiguous nuclear ROIs was isolated.
385 Nuclei were removed when the total number of 2D ROIs was less than 5. For each
386 nucleus, the ROI with the largest area was designated the nuclear midplane. Nuclei were
387 excluded if this ROI was at the top or bottom of the ROI stack. Nuclear volumes were
388 calculated as the sum of the volumes of nuclear ROI voxels (using the Z thickness
389 obtained after correction for axial distortion).

390 **Whole-cell 2D segmentation**

391 Initial whole-cell segmentation was accomplished by first reducing the brightfield
392 image Z-stack to the optical sections below the most in-focus optical section, which we
393 defined as the optical section for which the standard deviation of pixel intensities in the
394 image is minimized (Fig. S3). Since we used a microfluidics chamber in which cells form
395 a flat layer, we initially assumed that the most in-focus optical section is the same for all
396 cells in an image. A Gaussian blur was used on each optical section to reduce image
397 noise. An unsharp mask was used to enhance the acutance of the boundary band
398 surrounding each cell. An adaptive threshold (Otsu's method[49]) was used to produce a
399 binary image for each optical section. In optical sections close to the focal plane, cell
400 boundaries are hard to detect as the boundary band width approaches zero (Fig. S3A,

401 0 μm). The farther an optical section is from the focal plane, the larger the boundary band
402 width becomes (Fig. S3A, -2.4 μm). We therefore averaged the binary images from all
403 remaining optical sections to produce an image where boundary bands appear as
404 gradients, akin to valleys in a topographic map (Fig. 1B, panel 2). We interpret the darker
405 regions in this grayscale map to be high confidence areas for cell borders. An additional
406 adaptive threshold was used on this projection (Otsu's method[49]). Using these steps, cells
407 were surrounded by a boundary band (Fig. 1B, panel 3). Fiji's "Analyze Particle" tool was
408 used to translate the binary image into whole-cell ROIs, and a distance transform was
409 used to measure the thickness of the boundary bands. All ROIs were then enlarged by
410 the half-width of the boundary band (Fig. 1B, panel 4). An optional watershedding
411 algorithm (Watershed Irregular Features, BioVoxxel Toolbox[50]) in the pipeline allows for
412 separating unsegmented adjacent cells or regions.

413 Debris or cell features such as septa and vacuoles can introduce gaps or jagged
414 edges in the segmented brightfield binary. To compensate for this, a smoothing algorithm
415 was used. The smoothing algorithm closes gaps in the ROI that fall beneath a size
416 threshold defined by the user. Additionally, cells along the image periphery were excluded
417 based on a user-defined margin.

418 Adapted from the MAARs pipeline[13], an optional solidity filter was used to exclude
419 some ROIs that do not represent cells. An ROI's solidity is the ratio of its area and its
420 convex hull area, where a value of 1 indicates a completely convex object. We made this
421 step optional and adjustable, because, as also observed by Liu *et al.*[14], cells with
422 curvature may be falsely excluded while intercellular regions with high solidity may be
423 falsely included. An additional manual exclusion step allows users to remove falsely
424 included regions prior to 3D reconstruction.

425 Within the pipeline, whole-cell 2D ROIs are initially constructed in the optical
426 section that is considered the most in-focus for the entire image. However, this does not
427 always coincide with the optical section where the nucleus has its largest diameter (which
428 we consider the midplane for the nucleus). Differences between the nuclear and cellular
429 midplane position result in vertical misalignment between a nucleus and its enclosing cell.
430 As an additional optional step, when nuclear data are available, the whole-cell 2D ROI for

431 a given cell can therefore be re-assigned to the midplane of the corresponding nucleus,
432 which we did when nuclear measurements were available (Fig. 4, but not Fig. 5).

433 **Whole-cell 3D reconstruction**

434 We used the assumption that cells are radially symmetric around a central axis
435 along the length of the cell[39] to guide our whole-cell 3D reconstruction. To reconstruct
436 cells, we use the midplane ROI as the starting point. The reconstruction algorithm then
437 extrudes a series of spheres along the topological skeleton of the cell (Fig. 2A).

438 The Euclidean distance map and the topological skeleton were generated from the
439 binary midplane ROI. The Euclidean distance map is a greyscale image where the value
440 of each pixel is its Euclidean distance from the closest edge of the ROI (Fig. 1B, panel 6;
441 Fig. 2C). We used the Fiji implementation of an algorithm for generating a Euclidean
442 distance map[51]. The topological skeleton is a one-pixel-wide shape that is equidistant
443 from the boundaries of the ROI (Fig. 1B, panel 5). We used the Fiji legacy implementation
444 of a thinning algorithm[52] to produce topological skeletons. The union of the distance map
445 and topological skeleton yields a topological skeleton where each pixel along the skeleton
446 has a value representing the distance of the topological skeleton to the ROI boundary
447 (Fig. 1B, panel 7; Fig. 2C). For 3D extrusion (Fig. 2A), we centered spheres on these
448 pixels with the radius of the sphere taken from the distance value of each pixel (Fig. 2C,D).
449 Due to a limitation in Fiji's ROI system, ROIs are always two-dimensional, confined to a
450 single optical section. In order to construct a sphere, concentric, circular, cross-sectional
451 ROIs of the sphere are created whose radii are a function of the parent sphere's radius,
452 and the cross section's axial distance from the midplane (Fig. 2B). The cross-sectional
453 radii are given by

454 $$r = \sqrt{R^2 - \Delta z^2}$$

455 where r is the radius of the cross-section ROI, R is the radius of the parent sphere,
456 and Δz is the cross-section's distance from the midplane. Sub-pixel coordinates for these
457 cross-sectional ROIs were resolved by rounding to their nearest pixel coordinates
458 (Fig. 2B). The union of all coplanar circular cross sections forms the 2D ROI for a given
459 optical section. All 2D ROIs for a given cell were associated across optical sections to

form the whole-cell 3D ROI (Fig. 2E). The amount of detail in the reconstruction is proportional to the resolution of the imaging system (Fig. 2F). Whole-cell volumes were calculated as the sum of the volumes of whole-cell ROI voxels (using the Z thickness obtained after correction for axial distortion).

Nuclear and whole-cell intensities

To quantify fluorescent signal within ROIs, the 2D cross-sectional ROIs are used to measure the integrated density of each region. The integrated density across all cross-sections is summed up to produce the volumetric integrated density. To calculate mean intensity in each region, volumetric integrated density is divided by the volume of the 3D ROI.

Calculation of whole-cell volumes from idealized rod shape

To calculate shape descriptors for idealized, rod-shaped cells (Fig. 4A), we extracted cell length and width for these idealized cells from the midplane ROI using two different methods. The first method used the major and minor axes of an elliptical fit as cell length (*L*) and width (*W)*. The second method used the maximum and minimum Feret diameter (also called the caliper diameter) as length and width. The Feret/caliper diameter is the distance between two parallel lines tangential to the ROI. Cells were assumed to be rod-shaped, described as a cylinder with hemispheres at either end. The volume is given by:

$$V_{wholecell} = h\pi r^2 + \frac{4}{3}\pi r^3$$

where *h* is the length of the cylindrical body and *r* is the radius of the cell from the central axis. Radius and length of the cylindrical body were calculated from cell width and length as $r = W / 2$ *and* $h = L - 2r$.

Calculation of nuclear volumes from idealized elliptic shape

For nuclei, the longer (*L*) and shorter (*W*) diameter were determined by elliptical fit or Feret diameters, similar to the parameter extraction described for whole-cell idealized volumes. Volumes were calculated under the assumption of nuclei being ellipsoidal. The volume is given by:

488 $$V_{nucleus} = \frac{4}{3}\pi ab^2$$

489 with $a = L / 2$ and $b = W / 2$.

Acknowledgements

490 We thank the Nurse and Watanabe labs, as well as F. Obuekwe and
491 D. Weidemann for generating several strains used in these experiments, and
492 D. Weidemann for feedback on the pipeline. We thank J. Rogers and C. Morton for
493 assisting in experiments related to performance testing, E. Wood for recommendations
494 on microfluidics settings, and all members of the Hauf lab for comments on the
495 manuscript. We thank Wayne Rasband and the Image.sc Forum community for their
496 guidance and support.

497 **Funding**

498 Research reported in this publication was supported by the National Institute of
499 General Medical Sciences (NIGMS) of the National Institute of Health (NIH) under award
500 number R35GM119723 and by the National Science Foundation under Grant No.
501 1616247.

502 **Author Contributions**

503 Project administration and supervision: SH. Experiment design: EKB, EE, SH.
504 Imaging: EKB, EE. Pipeline programming: EKB. Pipeline testing and evaluation: EKB,
505 EE. Pipeline documentation: EKB. Manuscript writing: EKB. Manuscript revision: EKB,
506 SH.

507 **Additional Information**

508 The authors declare no competing interests.

509 **References**

510 1 Mattiazzi Usaj, M. *et al.* High-Content Screening for Quantitative Cell Biology. *Trends Cell*
511 *Biol* **26**, 598-611, doi:10.1016/j.tcb.2016.03.008 (2016).

2 McQuin, C. *et al.* CellProfiler 3.0: Next-generation image processing for biology. *PLoS Biol* **16**, e2005970, doi:10.1371/journal.pbio.2005970 (2018).

3 Schindelin, J. *et al.* Fiji: an open-source platform for biological-image analysis. *Nature Methods* **9**, 676, doi:10.1038/nmeth.2019 (2012).

4 Hayles, J. & Nurse, P. Introduction to Fission Yeast as a Model System. *Cold Spring Harb Protoc* **2018**, doi:10.1101/pdb.top079749 (2018).

5 Hoffman, C. S., Wood, V. & Fantes, P. A. An Ancient Yeast for Young Geneticists: A Primer on the Schizosaccharomyces pombe Model System. *Genetics* **201**, 403-423, doi:10.1534/genetics.115.181503 (2015).

6 Wood, V. *et al.* The genome sequence of Schizosaccharomyces pombe. *Nature* **415**, 871-880, doi:10.1038/nature724 (2002).

7 Lock, A. *et al.* PomBase 2018: user-driven reimplementation of the fission yeast database provides rapid and intuitive access to diverse, interconnected information. *Nucleic Acids Res* **47**, D821-D827, doi:10.1093/nar/gky961 (2019).

8 Hagan, I., Carr, A., Grallert, A. & Paul, N. *Fission yeast : a laboratory manual*. xiv, 487 pages : illustrations (some color) ; 29 cm (Cold Spring Harbor Laboratory Press, 2016).

9 Aravind, L., Watanabe, H., Lipman, D. J. & Koonin, E. V. Lineage-specific loss and divergence of functionally linked genes in eukaryotes. *Proc Natl Acad Sci U S A* **97**, 11319-11324, doi:10.1073/pnas.200346997 (2000).

10 Vo, T. V. *et al.* A Proteome-wide Fission Yeast Interactome Reveals Network Evolution Principles from Yeasts to Human. *Cell* **164**, 310-323, doi:10.1016/j.cell.2015.11.037 (2016).

11 Dietler, N. *et al.* YeaZ: A convolutional neural network for highly accurate, label-free segmentation of yeast microscopy images. *bioRxiv*, 2020.2005.2011.082594, doi:10.1101/2020.05.11.082594 (2020).

12 Dimopoulos, S., Mayer, C. E., Rudolf, F. & Stelling, J. Accurate cell segmentation in microscopy images using membrane patterns. *Bioinformatics* **30**, 2644-2651, doi:10.1093/bioinformatics/btu302 (2014).

13 Li, T. *et al.* MAARS: a novel high-content acquisition software for the analysis of mitotic defects in fission yeast. *Molecular Biology of the Cell* **28**, 1601-1611, doi:10.1091/mbc.e16-10-0723 (2017).

14 Liu, G., Dong, F., Fu, C. & Smith, Z. J. Automated morphometry toolbox for analysis of microscopic model organisms using simple bright-field imaging. *Biology Open* **8**, bio037788, doi:10.1242/bio.037788 (2019).

15 Peng, J. Y. *et al.* PombeX: robust cell segmentation for fission yeast transillumination images. *PLoS One* **8**, e81434, doi:10.1371/journal.pone.0081434 (2013).

548 16 Ren, H. *et al.* Cellbow: a robust customizable cell segmentation program. *bioRxiv*,
549 2020.2004.2021.052597, doi:10.1101/2020.04.21.052597 (2020).

550 17 Neumann, F. R. & Nurse, P. Nuclear size control in fission yeast. *The Journal of Cell*
551 *Biology* **179**, 593, doi:10.1083/jcb.200708054 (2007).

552 18 Pan, K. Z., Saunders, T. E., Flor-Parra, I., Howard, M. & Chang, F. Cortical regulation of
553 cell size by a sizer cdr2p. *Elife* **3**, e02040, doi:10.7554/eLife.02040 (2014).

554 19 Sakuno, T., Tada, K. & Watanabe, Y. Kinetochore geometry defined by cohesion within
555 the centromere. *Nature* **458**, 852, doi:10.1038/nature07876 (2009).

556 20 Julou, T. *et al.* Cell–cell contacts confine public goods diffusion inside Pseudomonas
557 aeruginosa clonal microcolonies. *Proceedings of the National Academy of Sciences* **110**,
558 12577, doi:10.1073/pnas.1301428110 (2013).

559 21 Navarro, F. J. & Nurse, P. A systematic screen reveals new elements acting at the G2/M
560 cell cycle control. *Genome Biol* **13**, R36, doi:10.1186/gb-2012-13-5-r36 (2012).

561 22 Cantwell, H. & Nurse, P. A homeostatic mechanism rapidly corrects aberrant
562 nucleocytoplasmic ratios maintaining nuclear size in fission yeast. *J Cell Sci* **132**,
563 doi:10.1242/jcs.235911 (2019).

564 23 Jorgensen, P. *et al.* The size of the nucleus increases as yeast cells grow. *Mol Biol Cell*
565 **18**, 3523-3532, doi:10.1091/mbc.e06-10-0973 (2007).

566 24 Höög, J. L. *et al.* Organization of Interphase Microtubules in Fission Yeast Analyzed by
567 Electron Tomography. *Developmental Cell* **12**, 349-361,
568 doi:10.1016/j.devcel.2007.01.020 (2007).

569 25 Wu, J.-Q. & Pollard, T. D. Counting Cytokinesis Proteins Globally and Locally in Fission
570 Yeast. *Science* **310**, 310, doi:10.1126/science.1113230 (2005).

571 26 Yam, C., He, Y., Zhang, D., Chiam, K. H. & Oliferenko, S. Divergent strategies for
572 controlling the nuclear membrane satisfy geometric constraints during nuclear division.
573 *Curr Biol* **21**, 1314-1319, doi:10.1016/j.cub.2011.06.052 (2011).

574 27 Wood, E. & Nurse, P. Pom1 and cell size homeostasis in fission yeast. *Cell Cycle* **12**,
575 3228-3236, doi:10.4161/cc.26462 (2013).

576 28 Pickering, M., Hollis, L. N., D'Souza, E. & Rhind, N. Fission yeast cells grow approximately
577 exponentially. *Cell Cycle* **18**, 869-879, doi:10.1080/15384101.2019.1595874 (2019).

578 29 Hayles, J. *et al.* A genome-wide resource of cell cycle and cell shape genes of fission
579 yeast. *Open Biol* **3**, 130053, doi:10.1098/rsob.130053 (2013).

580 30 Mata, J. & Nurse, P. tea1 and the microtubular cytoskeleton are important for generating
581 global spatial order within the fission yeast cell. *Cell* **89**, 939-949, doi:10.1016/s0092-
582 8674(00)80279-2 (1997).

583 31 Nurse, P. Genetic control of cell size at cell division in yeast. *Nature* **256**, 547-551,
584 doi:10.1038/256547a0 (1975).

585 32 Fantes, P. Epistatic gene interactions in the control of division in fission yeast. *Nature* **279**,
586 428-430, doi:10.1038/279428a0 (1979).

587 33 Abenza, J. F., Chessel, A., Raynaud, W. G. & Carazo-Salas, R. E. Dynamics of cell shape
588 inheritance in fission yeast. *PLoS One* **9**, e106959, doi:10.1371/journal.pone.0106959
589 (2014).

590 34 Lugagne, J. B. *et al.* Identification of individual cells from z-stacks of bright-field
591 microscopy images. *Sci Rep* **8**, 11455, doi:10.1038/s41598-018-29647-5 (2018).

592 35 Wang, L. *et al.* Segmentation of yeast cell's bright-field image with an edge-tracing
593 algorithm. *Journal of Biomedical Optics* **23**, 116503 (2018).

594 36 Facchetti, G., Knapp, B., Flor-Parra, I., Chang, F. & Howard, M. Reprogramming Cdr2-
595 Dependent Geometry-Based Cell Size Control in Fission Yeast. *Curr Biol* **29**, 350-358
596 e354, doi:10.1016/j.cub.2018.12.017 (2019).

597 37 Facchetti, G., Knapp, B., Chang, F. & Howard, M. Reassessment of the Basis of Cell Size
598 Control Based on Analysis of Cell-to-Cell Variability. *Biophys J* **117**, 1728-1738,
599 doi:10.1016/j.bpj.2019.09.031 (2019).

600 38 Zegman, Y., Bonazzi, D. & Minc, N. Measurement and manipulation of cell size
601 parameters in fission yeast. *Methods Cell Biol* **125**, 423-436,
602 doi:10.1016/bs.mcb.2014.10.011 (2015).

603 39 Chang, F. & Huang, K. C. How and why cells grow as rods. *BMC Biol* **12**, 54,
604 doi:10.1186/s12915-014-0054-8 (2014).

605 40 Zhou, Z. *et al.* The contractile ring coordinates curvature-dependent septum assembly
606 during fission yeast cytokinesis. *Mol Biol Cell* **26**, 78-90, doi:10.1091/mbc.E14-10-1441
607 (2015).

608 41 Wang, L. & Tran, P. T. Visualizing single rod-shaped fission yeast vertically in micro-sized
609 holes on agarose pad made by soft lithography. *Methods Cell Biol* **120**, 227-234,
610 doi:10.1016/B978-0-12-417136-7.00015-X (2014).

611 42 Petersen, J. & Russell, P. Growth and the Environment of Schizosaccharomyces pombe.
612 *Cold Spring Harb Protoc* **2016**, pdb top079764, doi:10.1101/pdb.top079764 (2016).

613 43 Team, R. C. R: A Language and Environment for Statistical Computing (Version 3.5. 2, R
614 Foundation for Statistical Computing, Vienna, Austria, 2018). *There is no corresponding*
615 *record for this reference.[Google Scholar]* (2019).

616 44 Wickham, H. *et al.* Welcome to the Tidyverse. *Journal of Open Source Software* **4**,
617 doi:10.21105/joss.01686 (2019).

618 45 Kassambara, A. ggpubr: 'ggplot2' Based Publication Ready Plots <https://CRAN.R-
619 project.org/package=ggpubr> (2020).

46 Kassambara, A. ggcorrplot: Visualization of a Correlation Matrix using 'ggplot2' <https://CRAN.R-project.org/package=ggcorrplot> (2019).

47 Ripley, B. D. & Venables, W. N. *Modern Applied Statistics with S*. Fourth edn, (Springer, 2002).

48 Auguie, B. gridExtra: Miscellaneous Functions for "Grid" Graphics <https://CRAN.R-project.org/package=gridExtra> (2017).

49 Otsu, N. A Threshold Selection Method from Gray-Level Histograms. *IEEE Transactions on Systems, Man, and Cybernetics* **9**, 62-66, doi:10.1109/TSMC.1979.4310076 (1979).

50 Brocher, J. in *European BioImage Analysis Symposium. Paris, France.*

51 Leymarie, F. & Levine, M. D. Fast raster scan distance propagation on the discrete rectangular lattice. *CVGIP: Image Understanding* **55**, 84-94, doi:10.1016/1049-9660(92)90008-q (1992).

52 Zhang, T. Y. & Suen, C. Y. A fast parallel algorithm for thinning digital patterns. *Commun. ACM* **27**, 236-239, doi:10.1145/357994.358023 (1984).

Baybay - Figure 1

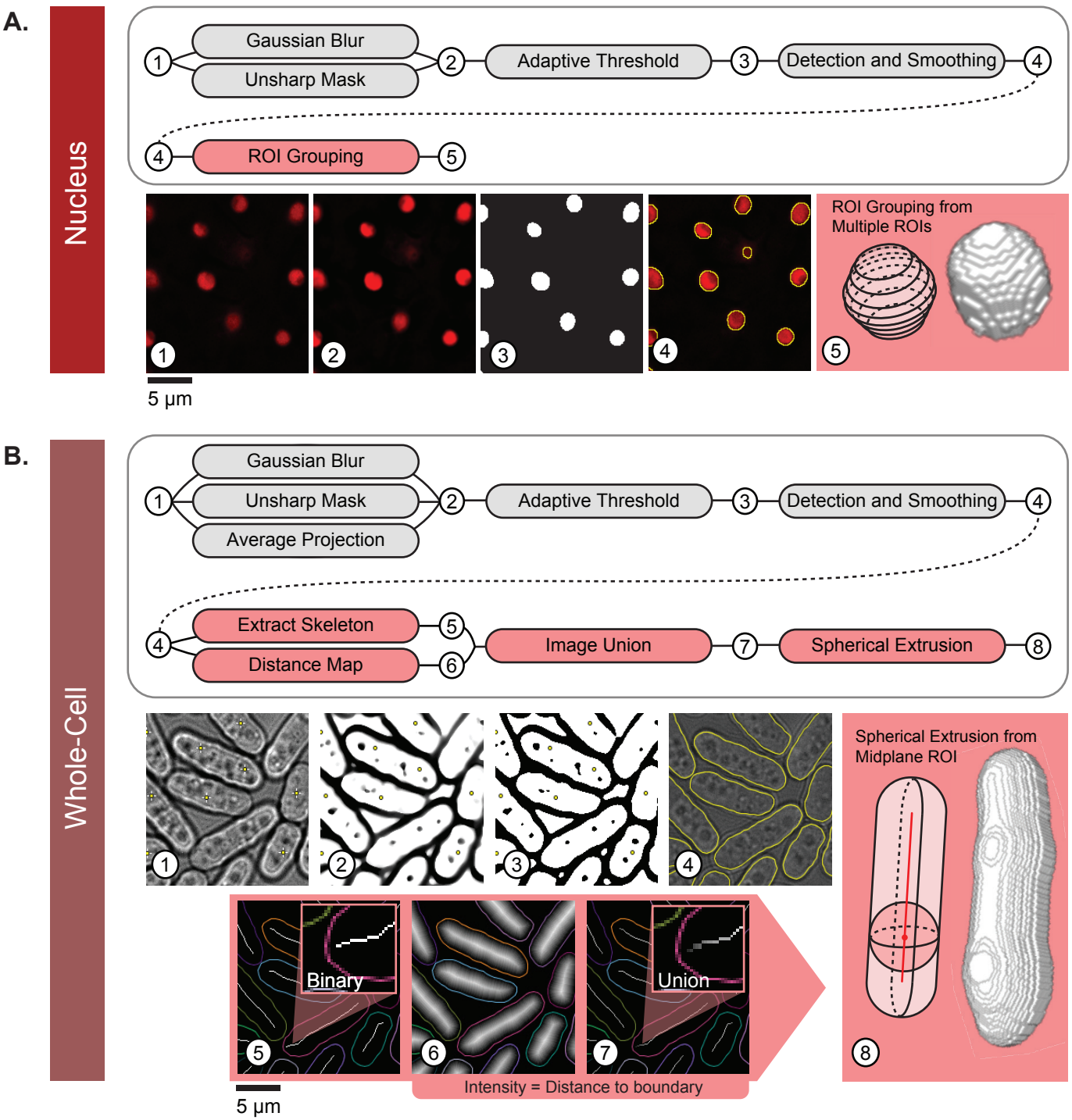

Figure 1. Pipeline Schematic

(A) Nuclear segmentation and reconstruction - (Top) Schematic of processing steps for 2D nuclear segmentation (grey) and 3D reconstruction (red). (Bottom) Sequential images through the segmentation and reconstruction process: (1) Sample slice of an input image, showing nuclear marker TetR-tdTomato-NLS, (2) Sample slice of a processed input image following Gaussian blur and unsharp mask, (3) Sample slice of a binary image from adaptive thresholding, (4) Smoothed ROIs derived from binary image, (5) Cartoon of reconstruction method and representative model from 3D reconstruction as a result of ROI grouping.

(B) Whole-cell segmentation and reconstruction - (Top) Schematic of processing steps for 2D whole-cell segmentation (grey) and 3D reconstruction (red). (1) Sample slice of an input bright-field image with point selection on nuclear centroids from A (for the optional alignment of whole-cell reconstructions in Z to the corresponding nuclei). (2) Z-projection of multiple slices processed with Gaussian blur and unsharp mask, (3) Binarization of projection, (4) Smoothed ROIs derived from binary image (yellow) overlaid with brightfield image, (5) Topological skeleton of binary, (6) Euclidean distance map of binary, (7) Union of topological skeleton and Euclidean distance map - used as radius profile input for spherical extrusion when generating the whole-cell 3D reconstruction, (8) Cartoon of reconstruction method and representative model from 3D reconstruction as a result of spherical extrusion. For simplicity, extrusion is shown here along a straight axis, but topological skeletons are typically not straight (panel 5,7).

Baybay - Figure 2

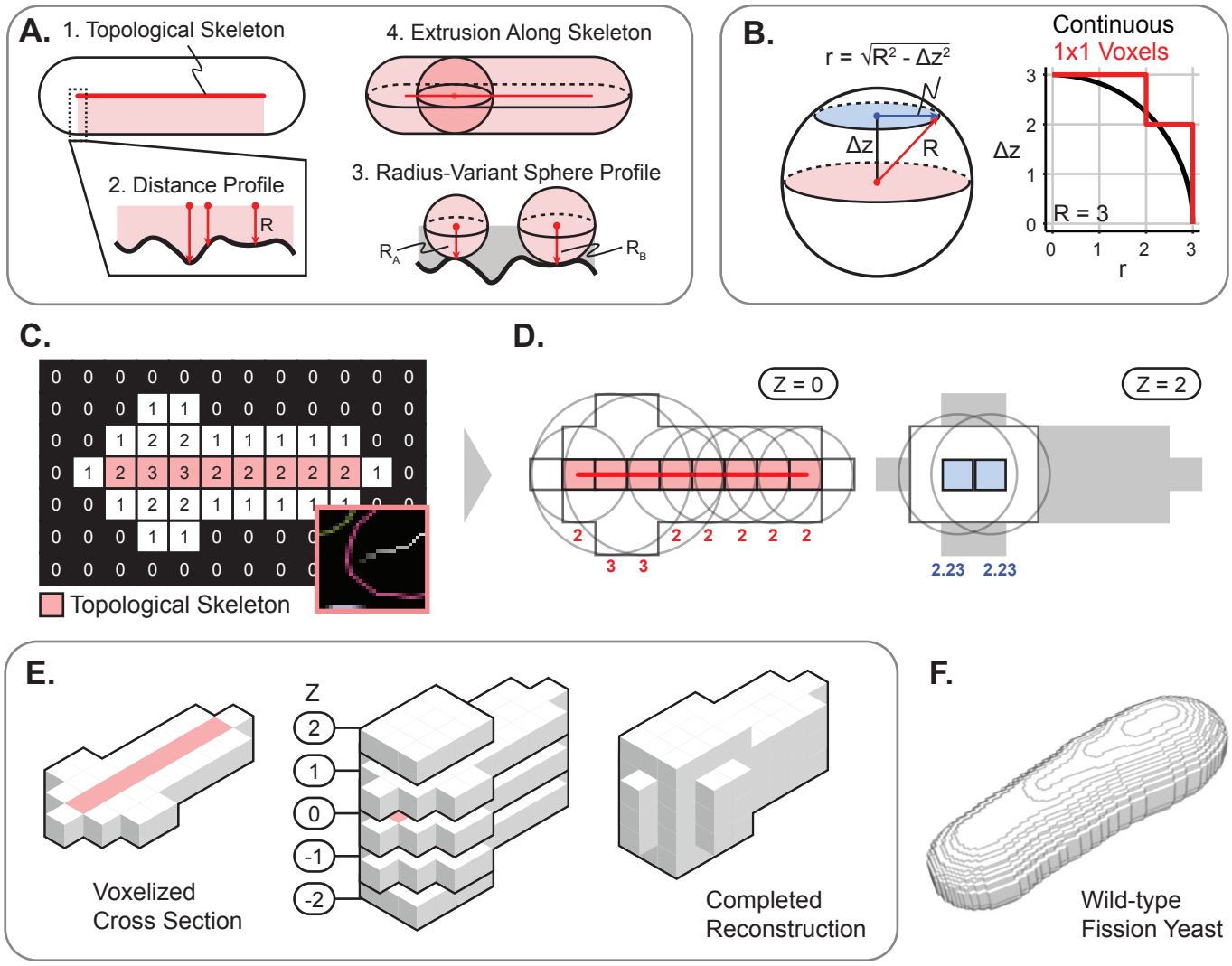

Figure 2. Whole-Cell Reconstruction Algorithm - (A) General schematic for the whole-cell 3D reconstruction algorithm: From a 2D binary image in the midplane of a cell, spheres are extruded along the topological skeleton, where the radii of these spheres is the distance to the nearest edge of the cell. Note that the topological skeleton is shown here as a straight line, but does not have to be straight. **(B)** At each optical section away from the midplane (distance: Δ z), a voxel is included in the reconstruction when the majority of its volume is part of the sphere profile. (Right) Black line represents the sphere profile, red line represents the voxelized z-section as seen in C. **(C)** Coarse 2D image converted into a distance map where the values in each pixel represent the Euclidean distance to the periphery of the binary, with the topological skeleton annotated in red. Inset: example of union between topological skeleton and distance map, from Figure 1B, panel 7. The greyscale of the pixels of the topological skeleton indicates distance to the periphery. **(D)** Sample points on topological skeleton at Z = 0 (left) and Z = 2 (right) with example spherical cross sections centered in XY along the topological skeleton. Cross section radii are determined by the equation described in (B). Radii are indicated in red at Z = 0 and blue at Z = 2. **(E)** Visualization of the coarse reconstruction in 3 dimensions, with all optical sections of the complete reconstruction shown. **(F)** Example 3D reconstruction of a wild-type cell (voxel size 0.1071 µm x 0.1071 µm x 0.065 µm).

Baybay - Figure 3

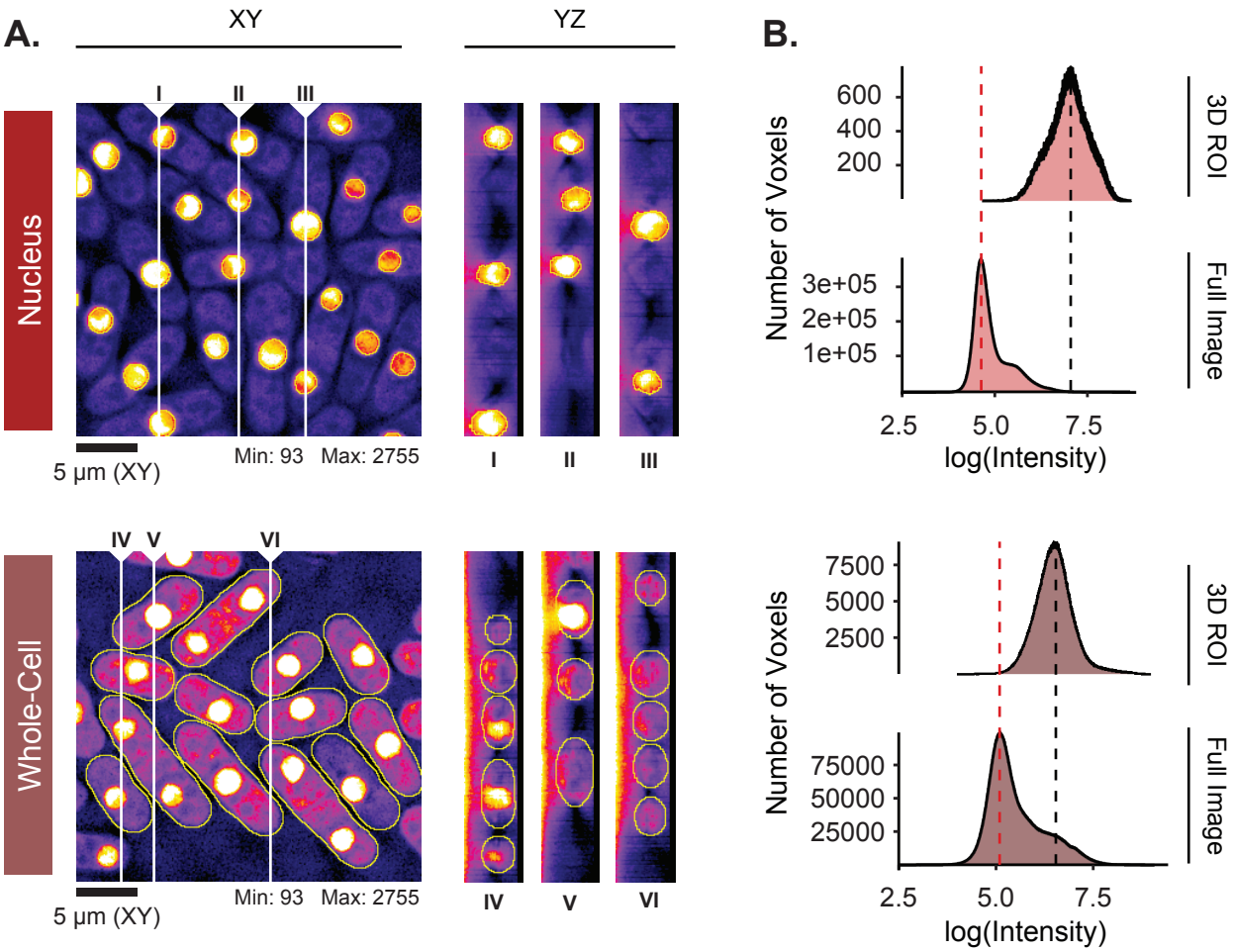

Figure 3. Signal Acquisition Performance - (A) Representative optical sections in XY and three sample YZ orthogonal views at different X positions. White vertical lines indicate sampling positions for corresponding YZ orthogonal views. Voxel size is 0.1071 µm x 0.1071 µm x 0.065 µm. Images are from fission yeast expressing TetR-tdTomato-NLS and Mep33-mCherry for nuclear analysis (top) and TetR-tdTomato-NLS and Mep33-tdTomato for whole-cell analysis (bottom). Annotations provide minimum and maximum intensities. All images have been subject to gamma correction (γ = 0.50) to improve visibility of cytoplasmic signal. **(B)** Intensity histograms for all voxels in the image (Full Image), and for all voxels contained within the 3D ROIs. Dashed lines annotate maxima: background (red) and signal of interest (black).

Baybay - Figure 4

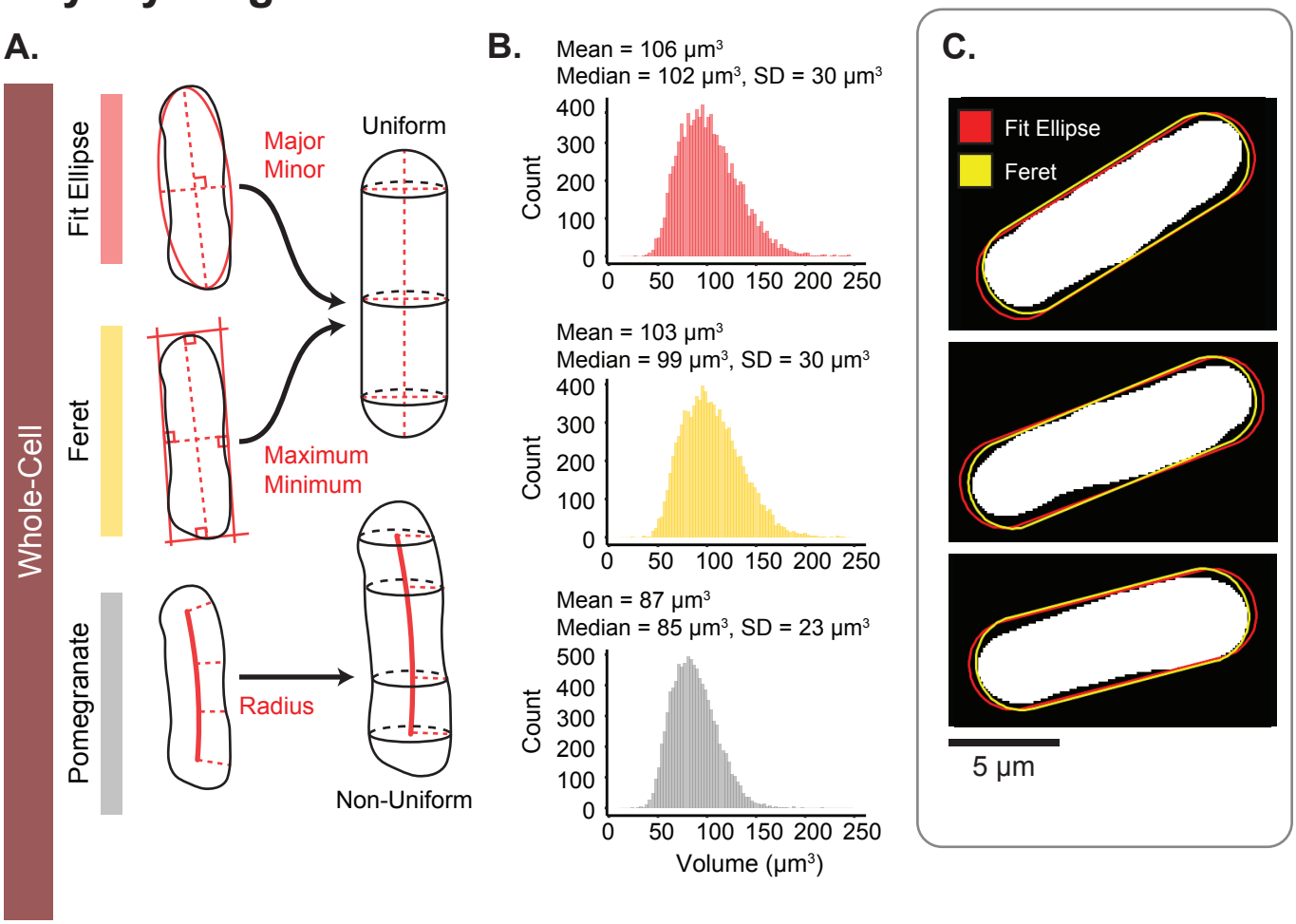

Figure 4. Comparison of Methods for Calculating Wild-Type Cell Volume - (A) Schematic representations of methods for calculating whole-cell volume. Parameters are extracted from the cell midplane (left), and used in generating 3D volume (right). The 'Fit Ellipse' method extracts the major and minor axes of an ellipsoidal fit as length and width, the 'Feret' method extracts the maximum and minimum Feret diameter as length and width. These are used as input to generate a rod-shaped cell. Pomegranate generates a non-uniform volume as described in Figure 2. **(B)** Histograms (binwidth = 3; Freedman-Diaconis) of cell volumes from the same population of 9329 cells, calculated with the three approaches: Fit Ellipse method (red); Feret method (yellow); and Pomegranate (grey). Annotations provide descriptive statistics (SD = standard deviation). **(C)** Midplane ROI (white), with overlaid cross sections of the rod-shape obtained with length and width from ellipse fitting (red) or Feret diameters (yellow). Three representative cells are shown.

Baybay - Figure 5

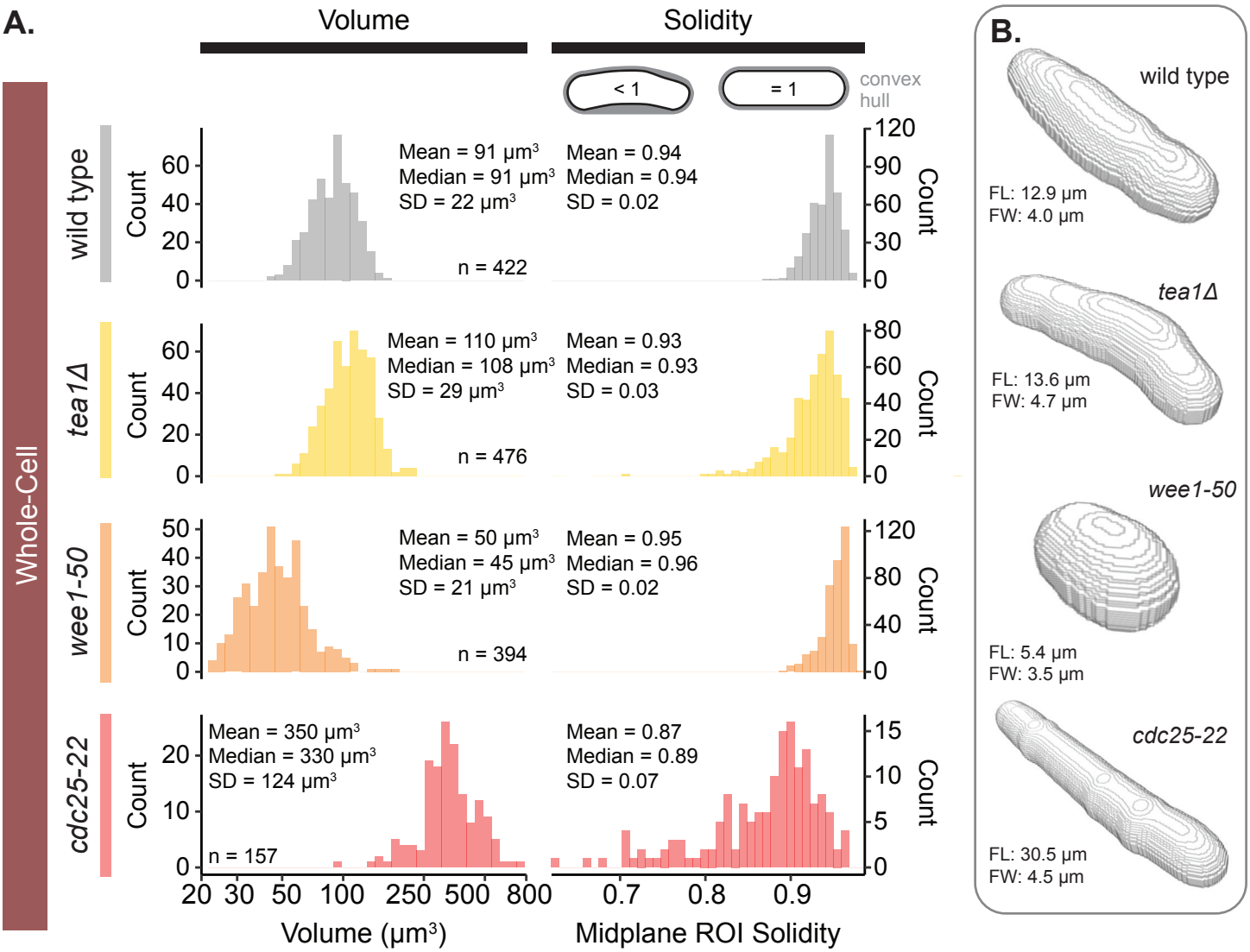

Figure 5. Size and Shape of Mutant Strains Captured by Pomegranate 3D Reconstruction - (A) Histograms (bins = 40) of volume (left) and midplane ROI solidity (right), representing size and curvature, respectively, for wild type and cell shape and cell size mutants. The x-axis of the volume histogram is on a base-10 logarithmic scale. Annotations provide descriptive statistics (SD = standard deviation). **(B)** Reconstruction models of representative, individual cells. Annotations provide size parameters for each cell to illustrate scale: maximum Feret diameter (Feret Length, FL) and minimum Feret diameter (Feret Width, FW).

Baybay - Figure 6

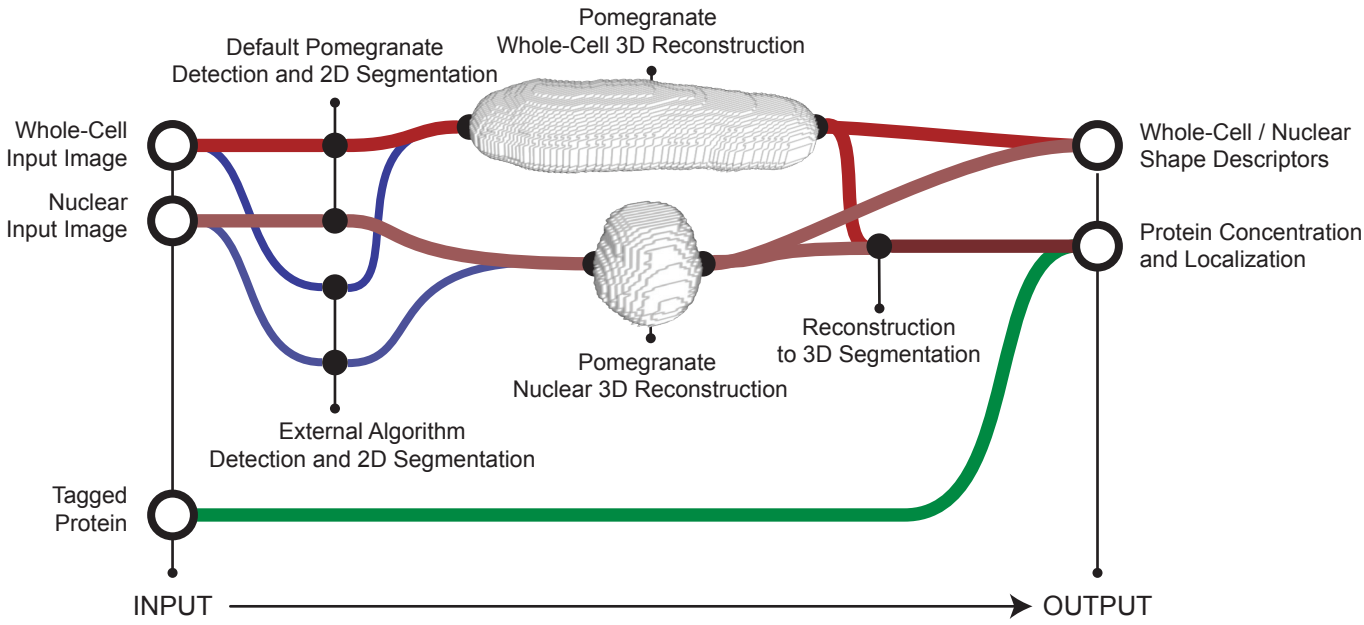

Figure 6. Workflow Schematic - General schematic of pipeline input and output. Reconstructions are not to scale. For detection and 2D segmentation, either Pomegranate or an external algorithm can be used. For Pomegranate 2D segmentation, a brightfield Z-stack is required as Whole-Cell Input Image, a fluorescence Z-stack is required as Nuclear Input Image. After reconstruction and 3D segmentation, any desired signal that was co-recorded ("Tagged Protein") can be quantified.

Baybay Figure S1

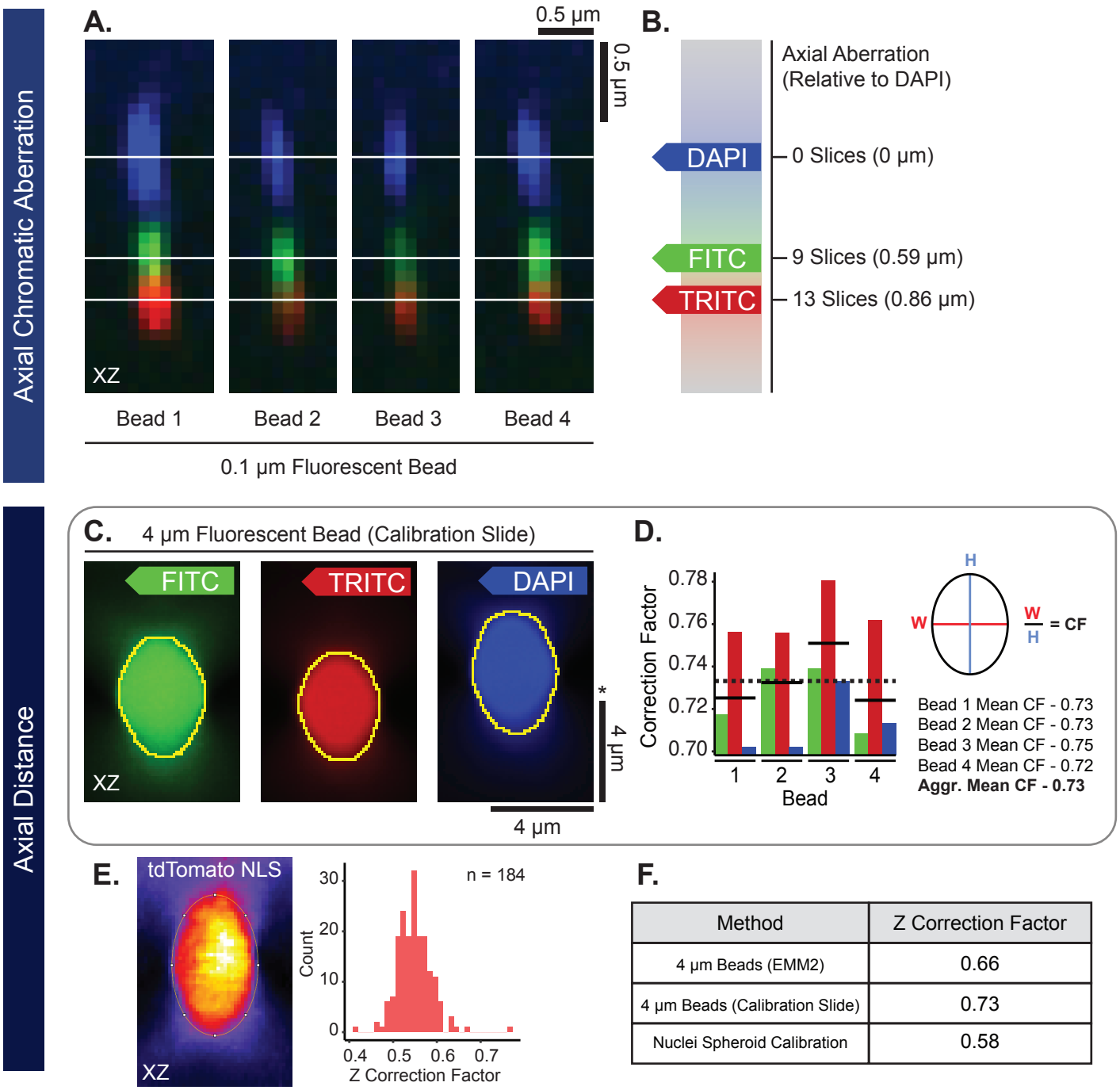

Method	Z Correction Factor
4 µm Beads (EMM2)	0.66
4 µm Beads (Calibration Slide)	0.73
Nuclei Spheroid Calibration	0.58

Supplemental Figure S1. Axial Corrections - Both axial chromatic aberration and distances need to be corrected for in order to obtain accurate quantifications of volume and fluorescence intensities. **(A)** Correcting for axial chromatic aberration: XZ maximum projections of 0.1 µm TetraSpeck Flourescent Microspheres. White bars are manually annotated midslices for each channel. Note that the vertical scale bar has been corrected with the appropriate axial distances (described in C-F). **(B)** Quantification of axial aberration relative to DAPI (blue fluorescence). **(C)** Sample axial distance calibration approach using fluorescent 4 µm beads. Shown are uncorrected XZ maximum projections of 4 µm TetraSpeck Fluorescent Microspheres. Note that the vertical scale bar (asterisk) represents uncorrected axial distance. **(D)** Bar plot of correction factors (CF) calculated as the aspect ratio (W/H, width/height) of the beads in XZ across multiple channels. Solid lines indicate mean CF for each bead, dashed line indicates mean CF across all beads (n = 4). **(E)** Alternative approach to axial distance calibration leveraging the assumption that nuclei are spherical in wild-type fission yeast: XZ maximum projection of a single fission yeast nucleus with TetR-tdTomato-NLS without correcting axial distance (left) and a histogram (bins = 30) of required CFs to yield spherical nuclei, from an image of 184 nuclei. **(F)** Table of Z correction factors derived from the methods described in C-E.

Baybay Figure S2

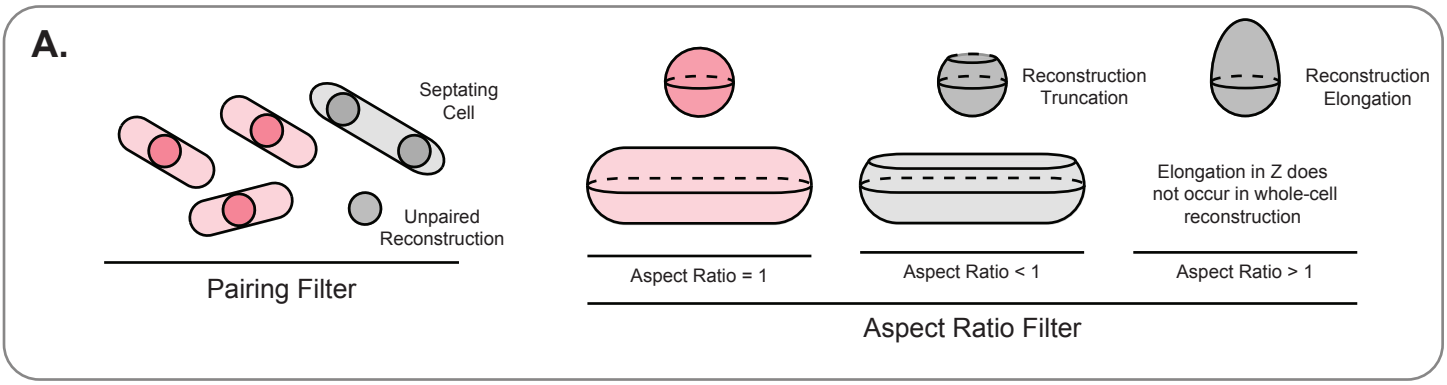

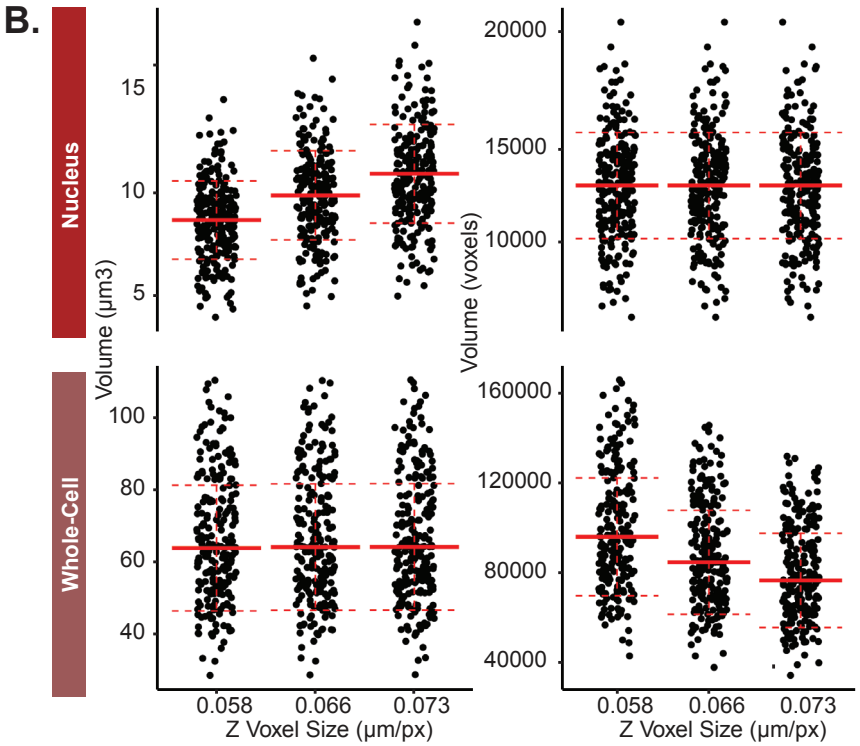

C.

Z	Volume	Nucleus Median	Nucleus SD	Whole-Cell Median	Whole-Cell SD
0.058	µm3	8.7	1.9	63.8	17.4
	voxels	13056	2858	95960	26117
0.066	µm3	9.9	2.2	64.1	17.5
	voxels	13056	2858	84673	23084
0.073	µm3	10.9	2.4	64.2	17.5
	voxels	13056	2858	76622	20896

Supplemental Figure S2. Comparison of Multiple Z Voxel Sizes - (A) Cartoon depicting the two common filters applied to Pomegranate outputs: Pairing and Aspect Ratio. The pairing filter lets only objects pass that contain one nuclear ROI and one whole-cell ROI. The aspect ratio filter is optional. Aspect ratio is calculated as the ratio of height in the Z direction against width in the XY plane. Only ROIs with aspect ratio between 0.8 and 1.2 are included. A low (<1) aspect ratio typically occurs when the midplane is not centered and not enough optical sections are available, so that the reconstruction is truncated. A high (>1) aspect ratio for nuclear ROIs typically occurs when background flouresence is mistakenly included. High aspect ratios do not occur whole-cell ROIs due to the radial symmetry of the spherical extrusion approach. **(B)** Plots of whole-cell and nuclear reconstruction volumes (both in cubic microns and in voxels) for identical sets of cells, processed in Pomegranate with different Z voxel sizes (determined from the analyses in S1) with data filtered as described in A. Each point represents one cell. Overlaid lines represent median (solid red line) and one standard deviation from the median (dashed red lines). Because of the different modes of 3D reconstruction, nuclear and cellular ROI voxel numbers and volumes in cubic microns are differently affected by the correction factors. **(C)** Table of descriptive statistics from (B) (SD = Standard Deviation).

Baybay Figure S3

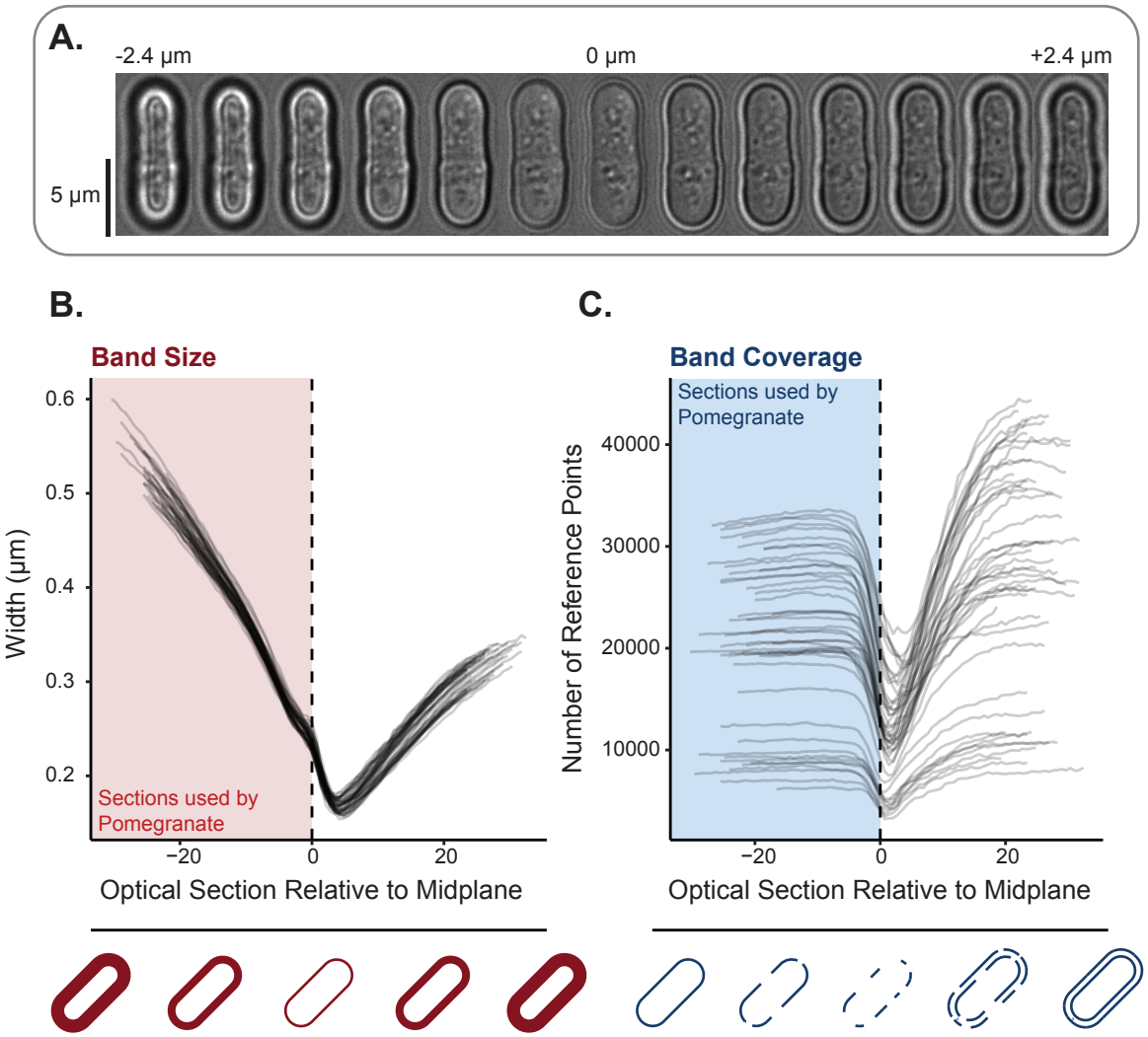

Supplemental Figure S3. Features of the Brightfield Image Z-stack - (A) Sample bright-field images at various optical sections in Z. **(B)** Line plot of mean black band width in a full field as a function of Z position, for multiple images. Shaded regions indicate the opticals sections used in Pomegranate's default 2D segmentation. The dashed line indicates the optical section in which the standard deviation of bright-field intensities is minimized – which we interpret as the most in-focus optical section. **(C)** Line plot of number of reference points used in black band width measurement in a full image as a function of Z position. The number of reference points is the number of pixels in the topological skeleton of a binarized black band (by adaptive threshold) – and is a metric of the overall length of the black band. The black band disappears as the bright-field image comes into focus. Dashed vertical line indicates the optical section in which the standard deviation of intensities is minimized. Schematic drawings at the bottom illustrate the reason for the changes in y-axis value.

Baybay Figure S4

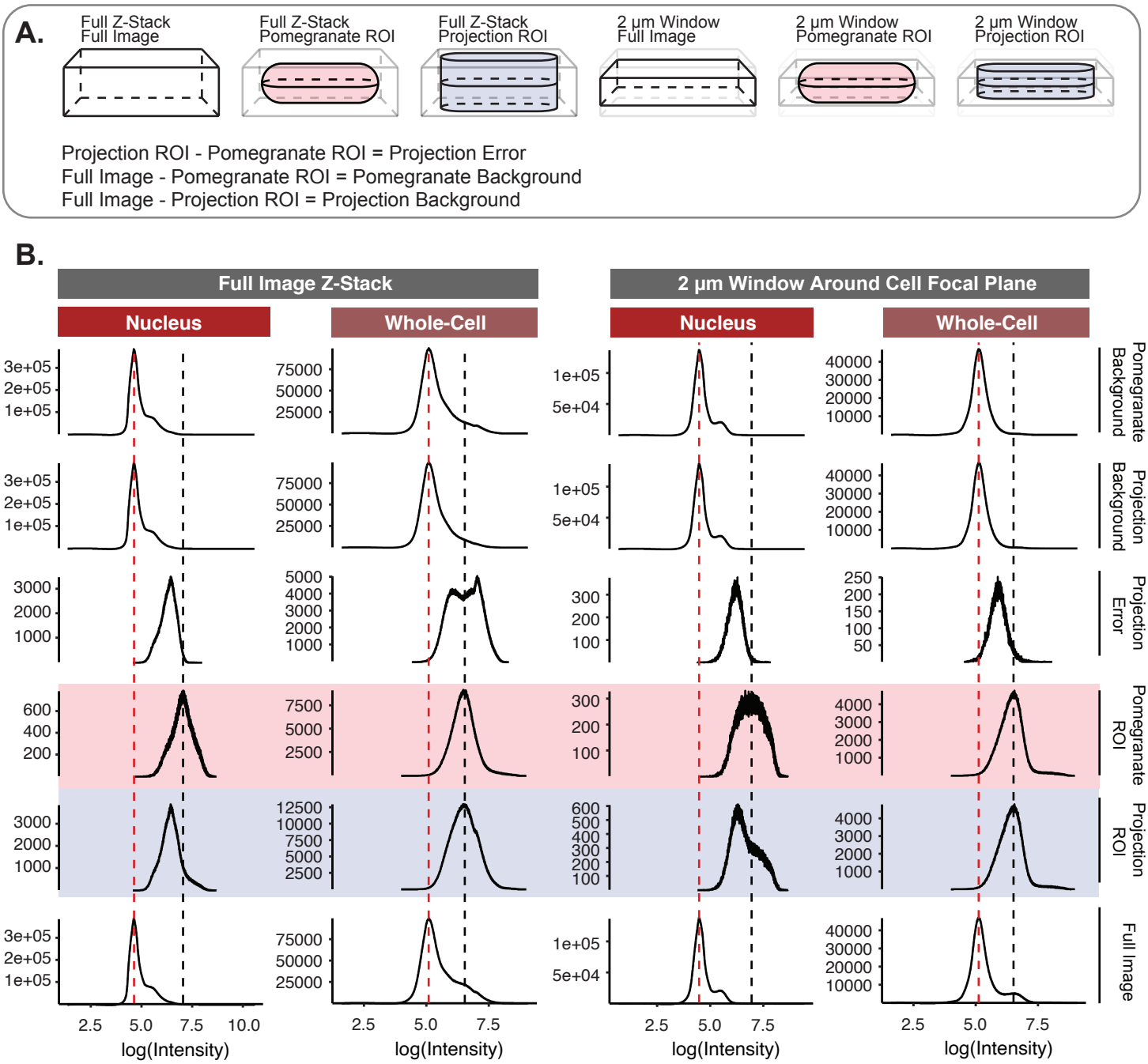

Supplemental Figure S4. Detailed Signal Acquisition Performance - (A) Cartoon representing regions described in the rows of B. 'Pomegranate ROI' refers to the output of Pomegranate's reconstruction algorithm. 'Projection ROI' refers to the region where the midplane ROI is used as ROI in all Z-sections. Projection error is the subtraction of signal acquired from Pomegranate's ROI from the signal acquired by the projection method. 'Pomegranate background' and 'Projection background' are the voxels in the full image not contained within either the Pomegranate ROI or the Projection ROI, respectively. Note that full images contain multiple cells. **(B)** Intensity histograms as in Figure 3B, with additional details. Either the full image Z-stack is used for analysis (left), or analysis is restricted to a 2 µm window in Z around the midplane (right). Dashed lines annotate maxima: background (red) and signal of interest (black). Use of projection collects lower intensities (likely extra-nuclear or extra-cellular) signals. Higher intensity signal acquired by the projection approach (seen as the second, higher-intensity maximum in the projection error in the full Z-stack) is likely caused by unbleached autofluorescence, which tends to disappear after a few exposures.

Baybay Figure S5

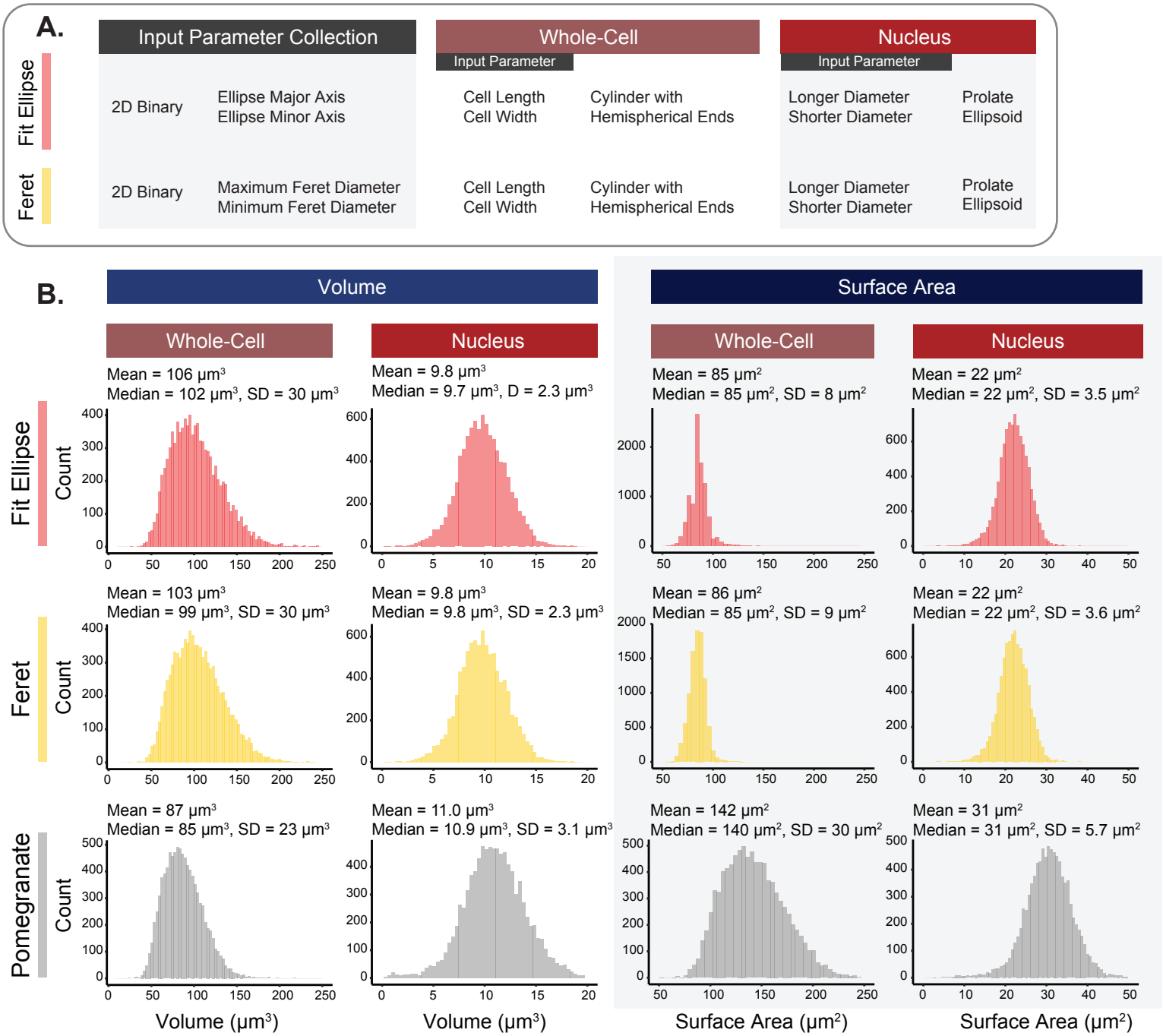

Supplemental Figure S5. Analysis of Volumes and Surface Areas - (A) Tabular schematic of idealized volume reconstruction approaches. For whole-cell idealized volumes, cell length and cell width are inputs for a rod-shaped geometry. Cell length and width are extracted from the 2D midplane ROI via the major and minor axes of a fit ellipse, or via the maximum and minimum Feret diameter, respectively. For nuclear idealized volumes, the longer and shorter diameter for the idealized nucleus are collected in the same way as for whole-cell ROIs using an elliptical fit and the Feret diameters. Longer and shorter diameter are inputs for a prolate ellipsoid with the longer diameter parallel to the cell midplane. **(B)** Histograms of whole-cell and nuclear volumes and surface areas of wild-type cells (n = 9329), comparing multiple strategies for reconstructing fission yeast volume. Whole-cell volume column binwidth = 3.0; Nuclear volume column binwidth = 0.36; Whole-cell surface area column binwidth = 4.0; Nuclear surface area column binwidth = 0.68 (Freedman-Diaconis). Annotations provide descriptive statistics (SD = Standard deviation). Volumes and surface areas for idealized volumes are calculated as a cylinder with hemispherical ends (cells) and prolate ellipsoid (nuclei). Pomegranate volumes and surface areas are derived from the Pomegranate reconstruction algorithm. Pomegranate volumes are given by the sum of the cross-sectional areas of all optical sections in a cell, multiplied by the spacing between optical sections in Z. Pomegranate surface area is given by the sum of perimeters of all optical sections in a cell, multiplied by the spacing between sections (lateral surface area) - added to the sum of all exposed top and bottom faces in the reconstruction - which is equal to two times the midplane cross-sectional area.

Baybay Figure S6

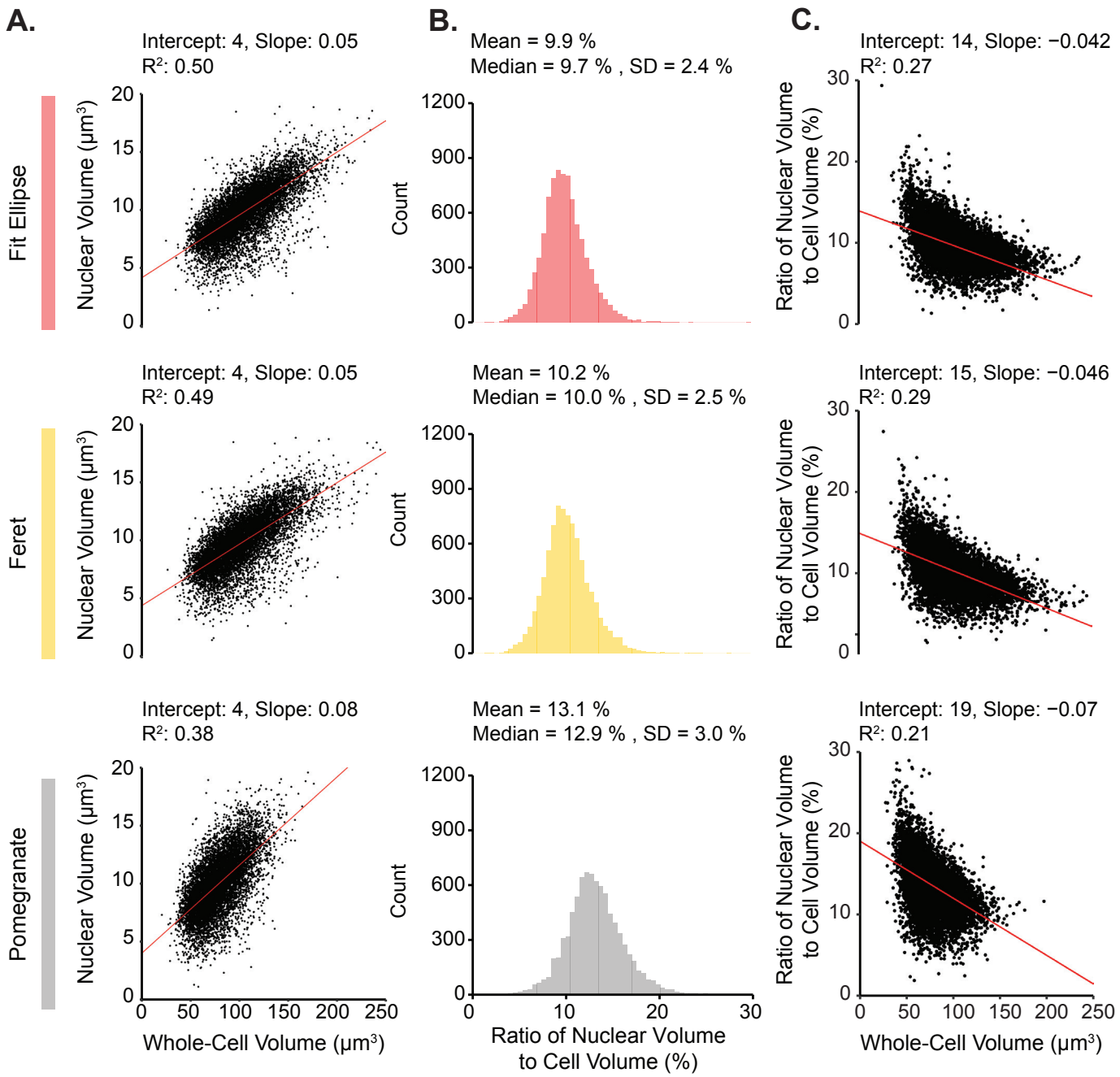

Supplemental Figure S6. Wild-Type Nuclear and Cell Volumes - The same population of cells shown in S5, subject to both filters described in S2A (n = 8627). **(A)** Nuclear and whole-cell volumes shown as scatterplots. Annotations provide information on the overlaid linear regression (red line). **(B)** Histograms of the ratio of nuclear volume to total cell volume as histograms (bins = 60). Ratios are calculated as the Pomegranate-reconstructed nuclear volumes divided by the whole-cell volumes derived from the various reconstruction methods. Annotations provide descriptive statistics (SD = Standard deviation). **(C)** Scatterplots of the ratio of nuclear volume to total cell volume, compared to total cell volume. Annotations provide information on the overlaid linear regression (red line).

Baybay Figure S7

A.

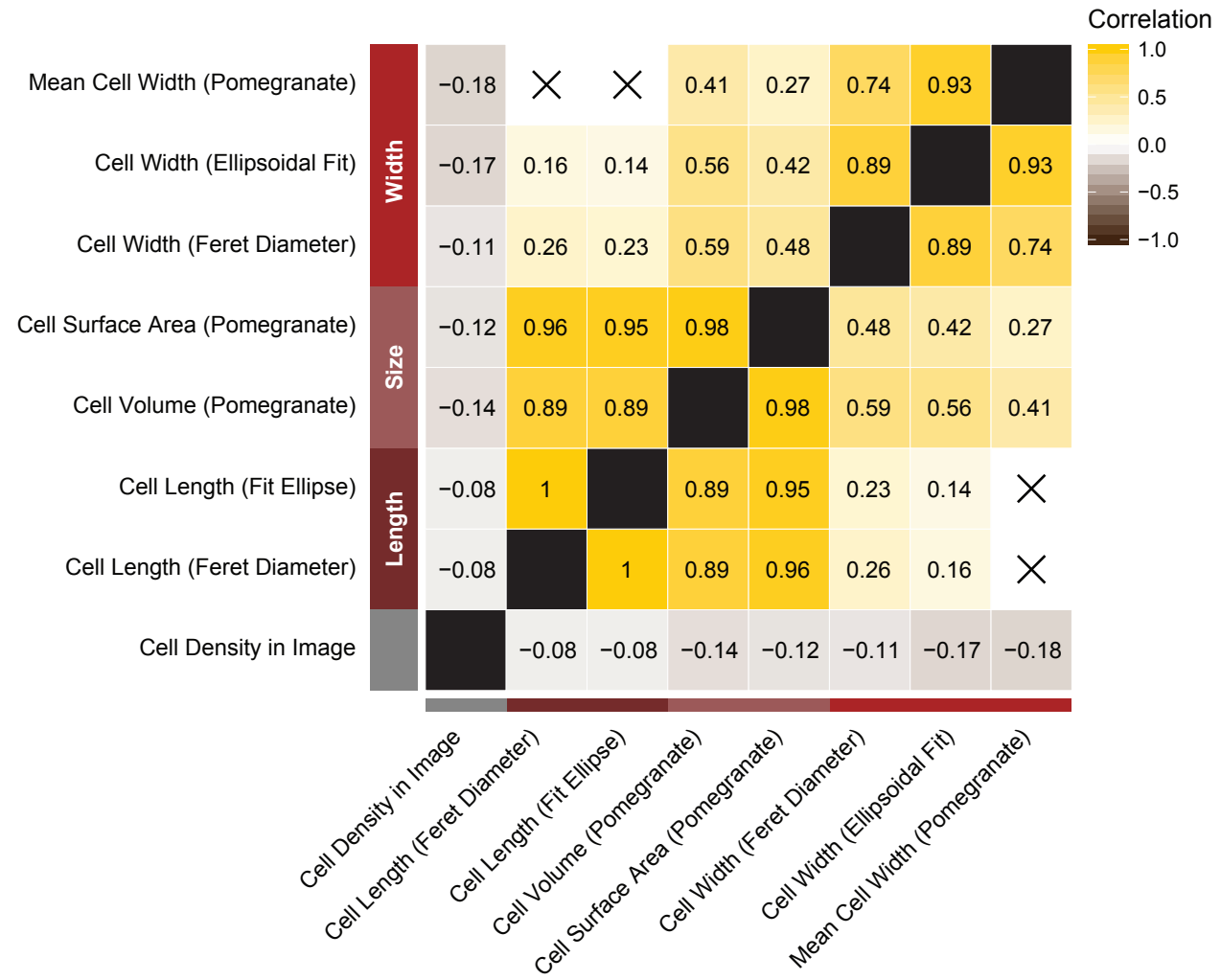

B.

Mean Cell Width (Pomegranate)	< 0.0001	0.5746	0.7369	< 0.0001	< 0.0001	< 0.0001	< 0.0001	
Cell Width (Ellipsoidal Fit)	< 0.0001	< 0.0001	< 0.0001	< 0.0001	< 0.0001	< 0.0001		< 0.0001
Cell Width (Feret Diameter)	< 0.0001	< 0.0001	< 0.0001	< 0.0001	< 0.0001		< 0.0001	< 0.0001
Cell Surface Area (Pomegranate)	< 0.0001	< 0.0001	< 0.0001	< 0.0001		< 0.0001	< 0.0001	< 0.0001
Cell Volume (Pomegranate)	< 0.0001	< 0.0001	< 0.0001		< 0.0001	< 0.0001	< 0.0001	< 0.0001
Cell Length (Fit Ellipse)	< 0.0001	< 0.0001		< 0.0001	< 0.0001	< 0.0001	< 0.0001	0.7369
Cell Length (Feret Diameter)	< 0.0001		< 0.0001	< 0.0001	< 0.0001	< 0.0001	< 0.0001	0.5746
Cell Density in Image		< 0.0001	< 0.0001	< 0.0001	< 0.0001	< 0.0001	< 0.0001	< 0.0001
	Cell Density in Image	Cell Length (Feret Diameter)	Cell Length (Fit Ellipse)	Cell Volume (Pomegranate)	Cell Surface Area (Pomegranate)	Cell Width (Feret Diameter)	Cell Width (Ellipsoidal Fit)	Mean Cell Width (Pomegranate)

Supplemental Figure S7. Correlation of Size Parameters - **(A)** Correlogram showing Person's r correlation coefficient on various combinations of size parameters, in addition to cell density in the image. Size parameters were extracted from the dataset presented in Figure S5 (n = 9329). X denotes relationships with non-significant correlation ($p > 0.05$). Cell length correlates strongly with Pomegranate reconstruction volume, as well as with theoretical volumes - supporting the preexisting concept that cell length is a viable approximation for cell size. However, the additional positive correlation between cell width and cell volume illustrates the importance of taking cell width into account when approximating cell size. **(B)** Table of p-values for the correlations presented in (A). Red cells indicate non-significant correlations ($p > 0.05$).

Baybay Figure S8

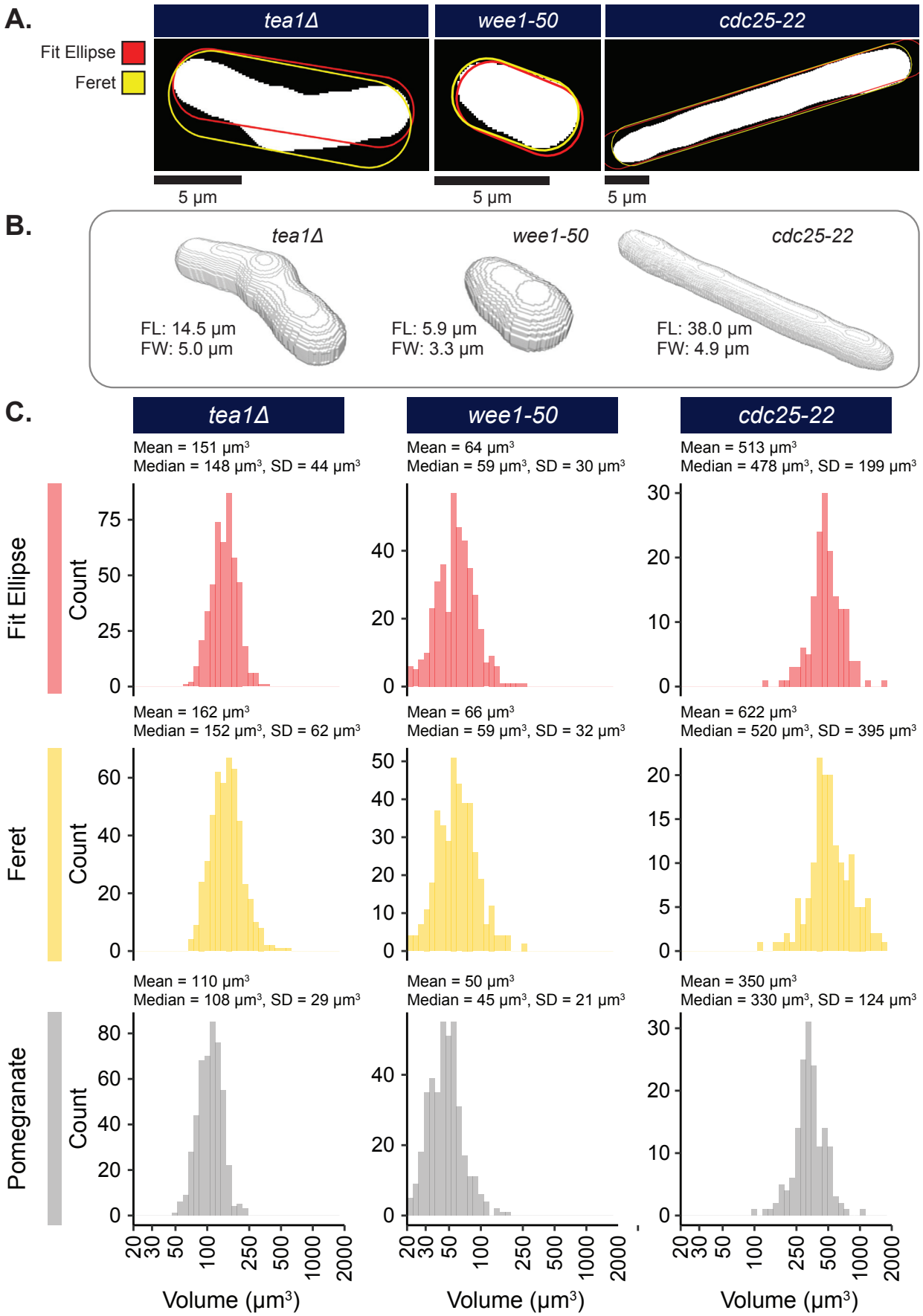

Supplemental Figure S8. Comparison of Methods for Calculating Cell Volumes in Size and Shape Mutants - (A) Midplane ROI (white), with overlaid cross sections of the rod-shape obtained with length and width from ellipse fitting (red) or Feret diameters (yellow). **(B)** Reconstruction models of representative, individual cells. Voxel size is 0.1071 µm x 0.1071 µm x 0.065 µm. Annotations provide size parameters for each cell: maximum Feret diameter (Feret Length, FL) and minimum Feret diameter (Feret Width, FW). **(C)** Histograms of whole-cell volumes for size and shape mutants produced with various reconstruction methods as described in Figure 4. The x-axis of the volume histogram is on a base-10 logarithmic scale. Annotations provide descriptive statistics (SD = Standard deviation, *tea1Δ*: n = 476 cells, *wee1-50*: n = 394 cells, *cdc25-22*: n = 157 cells).